ABSTRACT

Seismic Tomographic Imaging Reveals Possible Lithospheric Erosion
beneath Trans-Pecos Texas and Southeastern New Mexico

Carrie V. Rockett, M.S.

Advisor: Robert J. Pulliam, Ph.D

Results from the 1999-2001 La Ristra array revealed a fast seismic velocity anomaly beneath the Rio Grande rift, attributed to a lithospheric "drip" into the mantle, perhaps due to edge-driven convection. To investigate this anomaly, the *S*eismic *I*nvestigation of *E*dge-*D*riven *C*onvection *A*ssociated with the *R*io Grande Rift (SIEDCAR) project deployed a two-dimensional array of seismographs with a typical station spacing of ~35 km. Earthquakes of magnitude 5.0 or greater occurring at epicentral distances of 30- 90° were used to create tomographic images with FMTOMO. We present three-dimensional P and S tomographic models of the crust and upper mantle beneath the edge of the rift that confirm the anomaly's existence and show that it is more laterally extensive than was indicated previously. Our images reveal that the anomaly is disconnected from and adjacent to the Great Plains craton, suggesting convective lithospheric erosion is a likely cause of the fast seismic structure.

Seismic Tomographic Imaging Reveals Possible Lithospheric Erosion
beneath Trans-Pecos Texas and Southeastern New Mexico

by

Carrie V. Rockett, B.A.

A Thesis

Approved by the Department of Geology

Steven G. Driese, Ph.D., Chairperson

Submitted to the Graduate Faculty of
Baylor University in Partial Fulfillment of the
Requirements for the Degree
of
Master of Science

Approved by the Thesis Committee

Robert J. Pulliam, Ph.D., Chairperson

John A. Dunbar, Ph.D.

Gregory A. Benesh, Ph.D.

Accepted by the Graduate School
December 2011

J. Larry Lyon, Ph.D., Dean

Page bearing signatures is kept on file in the Graduate School.

TABLE OF CONTENTS

LIST OF FIGURES

ACKNOWLEDGMENTS

I would like to offer my deepest gratitude to my advisor Dr. Jay Pulliam for the numerous hours of guidance and assistance he has given me. I would like to give thanks to Dr. Steve Grand of the University of Texas at Austin for leading me to Baylor University and also for his guidance throughout my time here. For providing access to and troubleshooting for his personal cross-correlation program, I give thanks to Brandon Schmandt of the University of Oregon. I would also like to thank Yu Xia of UT-Austin for her assistance and company during my time in the field and for her contribution of receiver function analysis. I am very grateful for the time and patience offered by Sandy Suhardja of UT-Austin to teach me the tomographic inversion program. To my parents Dan and Kathy Rockett, my husband Ryan Lindsay, and fellow geophysicist Hallie Mintz, thank you for your endless support and for keeping me sane throughout the duration of my time at Baylor. For the installation and subsequent servicing of the SIEDCAR seismic stations, I would like to thank Dave Boyd, Tim Dillon, Tia Barrington,and the team of High School teachers who helped with SIEDCAR installation. Finally, I would like to thank EarthScope and IRIS/PASSCAL for their support and troubleshooting, and NSF for their funding of the project.

DEDICATION

To my husband and my parents

CHAPTER ONE

Introduction

Background

The Rio Grande rift is thought to mark the easternmost extent of deformation due to the subduction and foundering of the Farallon plate (*Dickinson and Snyder*, 1978; *Bunge and Grand*, 2000). The history of the region includes two episodes of continental extension accompanied by magmatism and uplift (*Baldridge et al.*, 1980; *Seager et al.*, 1984; *Baldridge et al.*, 1995). While it is likely that the cause of the first episode of extension was the foundering of the Farallon slab (*Humphreys*, 1995), the cause of the more recent episode remains in question. This recent regional tectonic and magmatic activity gives rise to many geological and geophysical questions. In particular, what is the relationship between processes in the Earth's mantle and at the surface? Do mantle processes have an effect on structure, uplift, and magmatism within the rift?

Tomographic results from La Ristra, a previous seismic deployment, show a fast seismic velocity anomaly beneath the eastern flank of the Rio Grande rift in southeastern New Mexico and West Texas (*Gao et al.*, 2004). However, this seismic array was linear and thus produced only 2D tomographic models. The spatial extent of the anomaly is therefore unknown. Furthermore, the anomaly was imaged at the southeastern-most edge of the array, where the model resolution is poorest. The hypothesis formed from the La Ristra results is that the fast anomaly is caused by the downwelling portion of a convection cell (*Gao et al.*, 2004) created by edge-driven convection (*van Wijk et al.*, 2008). This type of convection could be due to the step in lithospheric thickness from the thin material beneath the rift to the thicker cratonic material of the Great Plains (*King and Ritsema*, 2000; *van Wijk et al*., 2008). If this is the case, we would expect to see the downwelling extended to the north and south, following the edge of the Great Plains craton. Until the anomaly is imaged and quantified in three dimensions, its origin and effects on surface processes cannot be understood.

In 2004 EarthScope's USArray program began the deployment of a two dimensional seismic array consisting of 400 broadband seismometers (see *http://www.earthscope.org*). This Transportable Array (TA) is marching across the United States from west to east, allowing each station to remain in place for two years before it is re-deployed to the east. The TA was set for deployment in the Rio Grande rift region during 2008 – 2010, providing the opportunity for three-dimensional studies. Additional seismic stations were interspersed between TA stations to increase the array's resolution. These additional Flexible Array (FA) stations were deployed as a component of a project called *S*eismic *I*nvestigation of *E*dge-*D*riven *C*onvection *A*ssociated with the *R*io Grande Rift (SIEDCAR) (*Pulliam et al.*, 2009).

The purpose of our research is to utilize data from the densified seismic network to image beneath the eastern flank of the Rio Grande rift in southeastern New Mexico and west Texas using P- and S-wave traveltime tomography. Through these images we will first confirm the anomaly identified by the La Ristra deployment and associated studies (*Gao et al*., 2004; *West et al*., 2004; *Wilson et al*., 2005b) and, second, obtain three-dimensional, quantitative constraints on the geometry, size, location, and velocity contrast of the anomaly. These constraints will be useful in determining the origin or driving mechanism of the anomaly. Ultimately, the constraints obtained here will be used as input for future geodynamic modeling, which will further our understanding of the association of mantle and surface processes.

Geological History

The southwestern United States consists of a number of geological provinces that have been sutured together over the course of ~1.8 Ga. These provinces include the Yavapai, Mazatzal, and Grenville. The most recent suture zone connecting the Mazatzal and Grenville provinces trends northeastward through northern Chihuahua and West Texas and dates to approximately 1.1 Ga. This collisional event marked the final assembly of the southwestern portion of the North American craton (*Karlstrom and Humphreys*, 1998). Many of the tectonic features we now see in the southwestern United States (Fig. 1) are products of the subduction and subsequent foundering of the Farallon plate beneath the North American plate. Subduction occurred from approximately 80 to 40 Ma, during which time volcanism on the North American plate migrated eastward, suggesting relatively shallow subduction (*Coney and Reynolds*, 1977; *Dickinson and Snyder*, 1978). Foundering of the plate, beginning approximately 40 Ma is thought to have initiated extension within the Rio Grande rift and the Basin and Range Province (*Keller and Baldridge*, 1999). A zone of pre-existing crustal deformation caused by the Laramide event (40-50 Ma) likely dictated the location of rifting (*Baldridge et al.*, 1995). The second episode of extension commenced after a brief lull in regional tectonic and magmatic activity from ~20 to ~10 Ma (*Chapin and Seager*, 1975; *Chapin*, 1979; *Baltz*, 1978; *Manley*, 1979; *Manley and Mehnert*, 1981; *Golombek et al.*, 1983; *Seager et al.*, 1984; *Morgan et al.*, 1986). Regional uplift has been associated with extension, and since about 13 Ma, the northern Rio Grande rift and Southern Rockies have experienced an estimated uplift of approximately 1.1 km (*Axelrod and Bailey,* 1976; *Morgan et al*., 1986; *Eaton*, 1986). Though some have attributed this uplift to fault movement during the second episode of rifting, the evidence is inconclusive (*Chapin and Seager,* 1975; *Chapin,* 1979; *Morgan et al.,* 1986).

Volcanic activity throughout the southwestern U.S. accompanied both the initial stage of rifting about 35 - 20 Ma as well as the second stage ~10 to ~3 Ma. The intermediate to silicic composition of early-stage volcanics suggest the magmatism was sourced by mantle lithosphere while recent magmatism appears to have been derived from the asthenosphere (*Perry et al.,* 1988; *Baldridge et al.,* 1991). This shift in magmatic source suggests that crust beneath the rift has been thinned by about 50 km between the first to second magmatic episodes (*Baldridge et al.,* 1991). Most recent volcanism trends northeast along what is called the Jemez Lineament (Fig. 1) (*Baldridge et al.,* 1991).

The Rio Grande rift acts as a boundary between the tectonically altered crust to the west and the more stable crust of the Great Plains to the east. This boundary is quite distinct to the north but becomes diffuse southward where it is bounded to the west by the Basin and Range Province and to the east by the Great Plains of West Texas. *Seager and Morgan* (1979) suggest that the rift extends to the southeastern end of the Presidio Basin in West Texas and northeastern Chihuahua. The thermo-tectonic system associated with the rift seems to die out in this area. The boundary between the Basin and Range Province and the southern Rio Grande rift is complex, but there are physiographic differences between the two. *Eaton* (2008) points out that mountain ranges associated

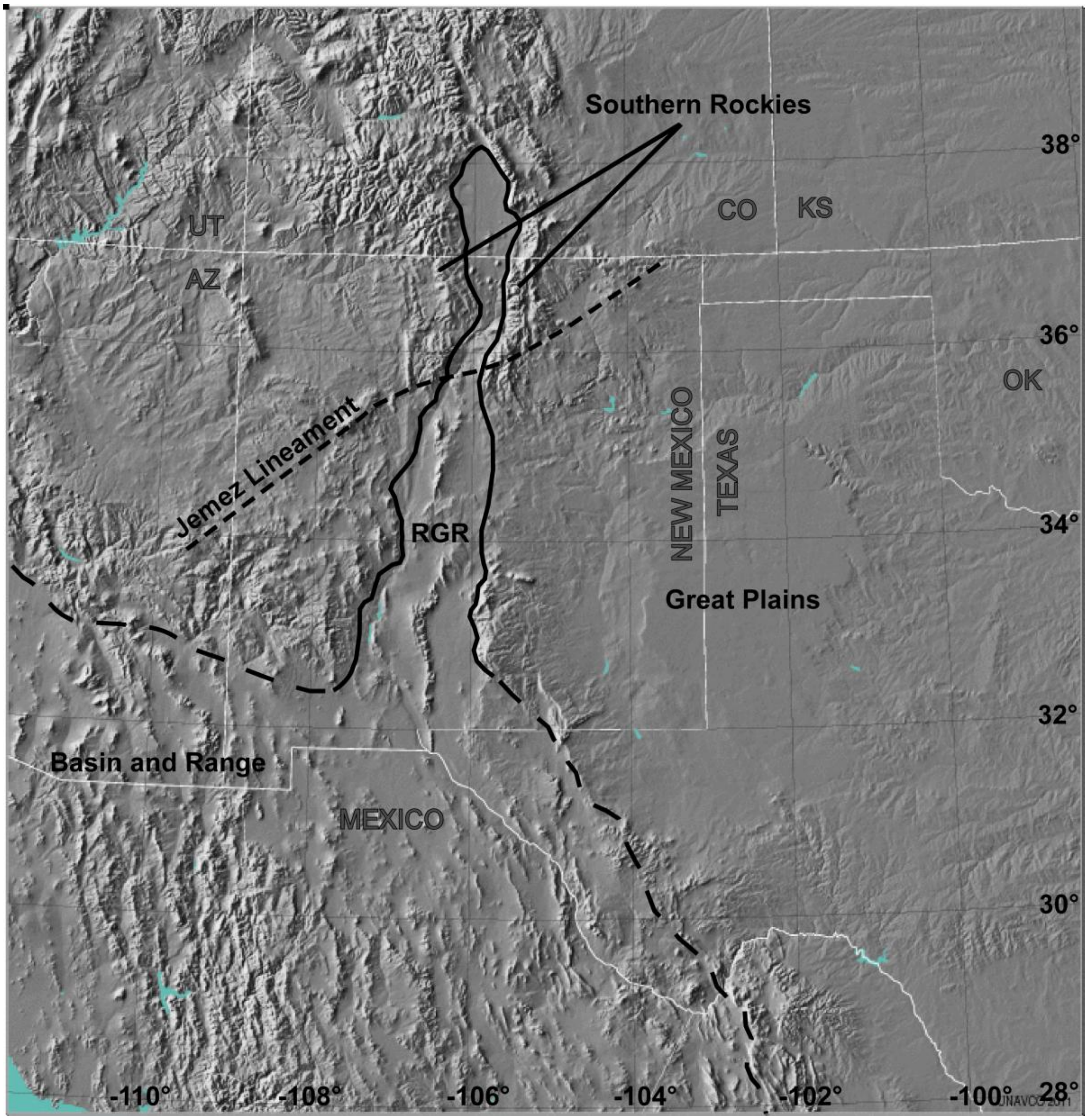

Figure 1. Shaded relief map showing the location of the Rio Grande rift (RGR) and surrounding physiographic provinces. Dashed lines indicate approximate locations.

with the Basin and Range strike approximately N55W while those associated with the rift trend north-south. This difference in extensional stress direction sets the two provinces apart. Though the boundary between the provinces is debated, there is no doubt that both were created during the same extensional event.

The southwest United States portrays a diverse geology. There is widespread agreement that there were two episodes of extension and magmatism within the rift; however, certain aspects of the rift's history remain in debate. Particularly, the cause of the second episode of rifting and its associated uplift is unclear. How these surface processes are connected to mantle processes is even less clear.

Previous Geophysical Work

The unique juxtaposition of geological provinces in the southwestern United States has warranted numerous geophysical studies throughout the region. Crustal and upper mantle structure has become more highly resolved and thus better understood through these studies. Geothermal studies dating back to 1975 show a northward-narrowing band of high heat flow along the axis of the Rio Grande rift extending from southern-central Colorado and northern-central New Mexico into northern Chihuahua, Mexico and West Texas (*Decker and Smithson*, 1975; *Reiter et al.*, 1975, 1978, 1979; *Smith and Jones*, 1979; *Swanberg*, 1979; *Clarkson and Reiter*, 1984; *Decker et al.*, 1984 1988). Bouguer gravity anomaly maps show a gravity low associated with the rift which narrows to the north and broadens to the south (*Cordell et al.*, 1982; *Keller and Cordell*, 1984; *Roy et al.*, 2005), a gravity signature similar to that of the East African rift (*Seager and Morgan*, 1979). The gravity low corresponds to a low seismic velocity zone in the upper mantle beneath the rift implying lithospheric thinning (*Davis et al.*, 1993).

Lithospheric thinning has similarly been interpreted from gravity data from the Kenya rift (*Girdler et al.* 1975; *Seager and Morgan*, 1979). Seismic refraction (*Olsen et al.*, 1979*; Sinno et al.*, 1986; *Murphy*, 1991), reflection (d*e Voogd et al.*, 1986, 1988), and surface wave dispersion (*Keller et al.*, 1979*; Sinno and Keller*, 1986) studies have confirmed the thinning of the lithosphere beneath the rift to 32-35 km.

The two-year La Ristra (Colorado P*la*teau/Rio Grande *Ri*ft *S*eismic *Tra*nsect Experiment) deployment spanned the rift from the Colorado Plateau in southeastern Utah to the Great Plains in west Texas (Fig. 2a). P and S tomographic models resulting from the La Ristra transect indicate a fast seismic velocity anomaly (labeled *C* in Fig. 2b,c) beneath the eastern edge of the Rio Grande rift (*Gao et al.*, 2004). This anomaly appears deeper and more significant in the shear wavespeed perturbation than in the compressional wavespeeds and indicates particularly high velocities at depths greater than 120 km. The inversion used by *Gao et al.* (2004) did not account for variations in anisotropy, which may explain the significant differences between their shear and compressional models. *Gao et al.* (2004) interpret this anomaly as the downwelling portion of a convection cell.

The origin of the anomaly described by *Gao et al.* (2004) cannot be determined confidently without knowledge of its thermal and compositional properties. Waveform modeling results by *Song and Helmberger* (2007) imply that the fast seismic velocity anomaly seen in the La Ristra results is not only thermally, but also compositionally distinct from the surrounding material. They suggest a temperature

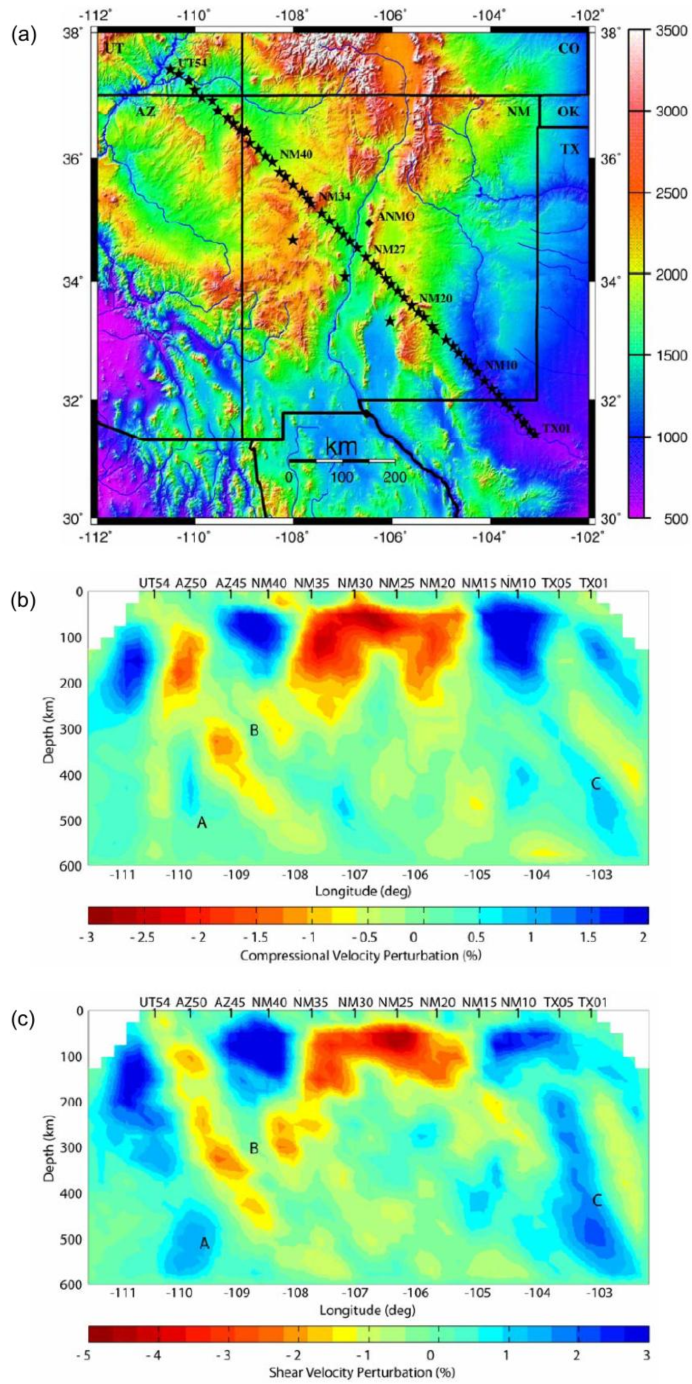

Figure 2. (a) Black stars denote the locations of stations in the linear La Ristra array. (b) A vertical cross-section showing the compressional velocity perturbation along the transect. (c) A vertical cross-section showing the shear velocity perturbation along the transect. In the cross-sections, A, B, and C are anomalous seismic velocity zones. Fast anomaly A is attributed to the foundering of the Farallon plate. Slow anomaly B is attributed to upwelling mantle, possibly due to volatile release from the Farallon plate. Fast anomaly C is of unkown origin (modified from *Gao et al.*, 2004).

difference of 310 ± 20°C between the anomaly and the warmer adjacent asthenosphere. They also show that the anomalous material is depleted; it has a ΔMg# (Mg / (Mg + Fe) × 100) of about 3. This number is consistent with Mg# variations in mantle asthenosphere and sub-continental lithosphere, as seen in xenolith and xenocryst analyses (*Lee at al.,* 2001; *Griffin et al.,* 2004; *O'Reilly and Griffin,* 2006; *Song and Helmberger,* 2007). *Song and Helmberger* (2007) claim that these thermal and compositional contrasts are sufficient to promote lithospheric erosion or small-scale edge-driven convection.

Geodynamic models indicate that small-scale edge-driven convection is likely to occur at the transition from thinned, extended lithosphere to thicker cratonic material. The convection cell created at such a transition zone is induced by lateral temperature and viscosity variations within the lithosphere and has been termed edge-driven convection (*King and Ritsema*, 2000*; van Wijk et al.*, 2008). Modeling by *King and Ritsema* (2000) and *van Wijk et al.* (2008) suggests that the downwelling portion of such a convection cell lies beneath the craton. The two-dimensional temperature variation models by *van Wijk et al.* (2008) were created with quantitative constraints from the La Ristra deployment and assume that the Rio Grande is a passive rift. The model that best reflects the geometry of the rift was obtained using an initial cratonic lithospheric thickness of 150 km east of the rift axis, a step decrease in lithospheric thickness of 40 km at the rift-craton transition, and a 2 mm/yr extensional velocity over the period of 25 million years (Fig. 3). Their research shows that a fast seismic velocity anomaly of the size and magnitude seen in the La Ristra results can be attributed solely to thermal contributions (e.g., cold downwelling).

Because the process of edge-driven convection is dependent on lithospheric structure, it is necessary to investigate the structure of the Moho beneath the region. Receiver function analysis on the La Ristra line by *Wilson et al.* (2005a, 2005b) show the crust has thinned to ~35 km at the center of the rift with an increase to 41-48 km beneath the Great Plains. Recent-, three-dimensional receiver function analysis using the SIEDCAR data shows a crust of 38-42 km beneath the rift and anywhere from 36 to 52 km beneath the Great Plains (Yu Xia, pers. comm., November 11, 2010). Xia's results indicate highly variable depths beneath both the rift and the craton, with generally greater depths beneath the craton. Highly variable depths are to be expected in Xia's case because of the large area covered in contrast to the linear space covered by La Ristra. Both of these studies agree with rift thicknesses found in previous studies (*Olsen et al.*, 1979; *Sinno et al.*, 1986; *Murphy*, 1991; *de Voogd et al.*, 1986, 1988; *Keller et al.*, 1979; *Sinno and Keller*, 1986) and confirm a step in crustal thickness up to ~10 km from the rift to the craton.

Geophysical studies of the Rio Grande rift and its surrounding regions seem to promote the hypothesis that edge-driven convection is the cause of the fast seismic anomaly seen in La Ristra results. However, none of these studies have assessed the three-dimensional geometry of the anomaly. Without three-dimensional constraints, we cannot fully understand the origin of the anomaly or the association it may have with surface geology.

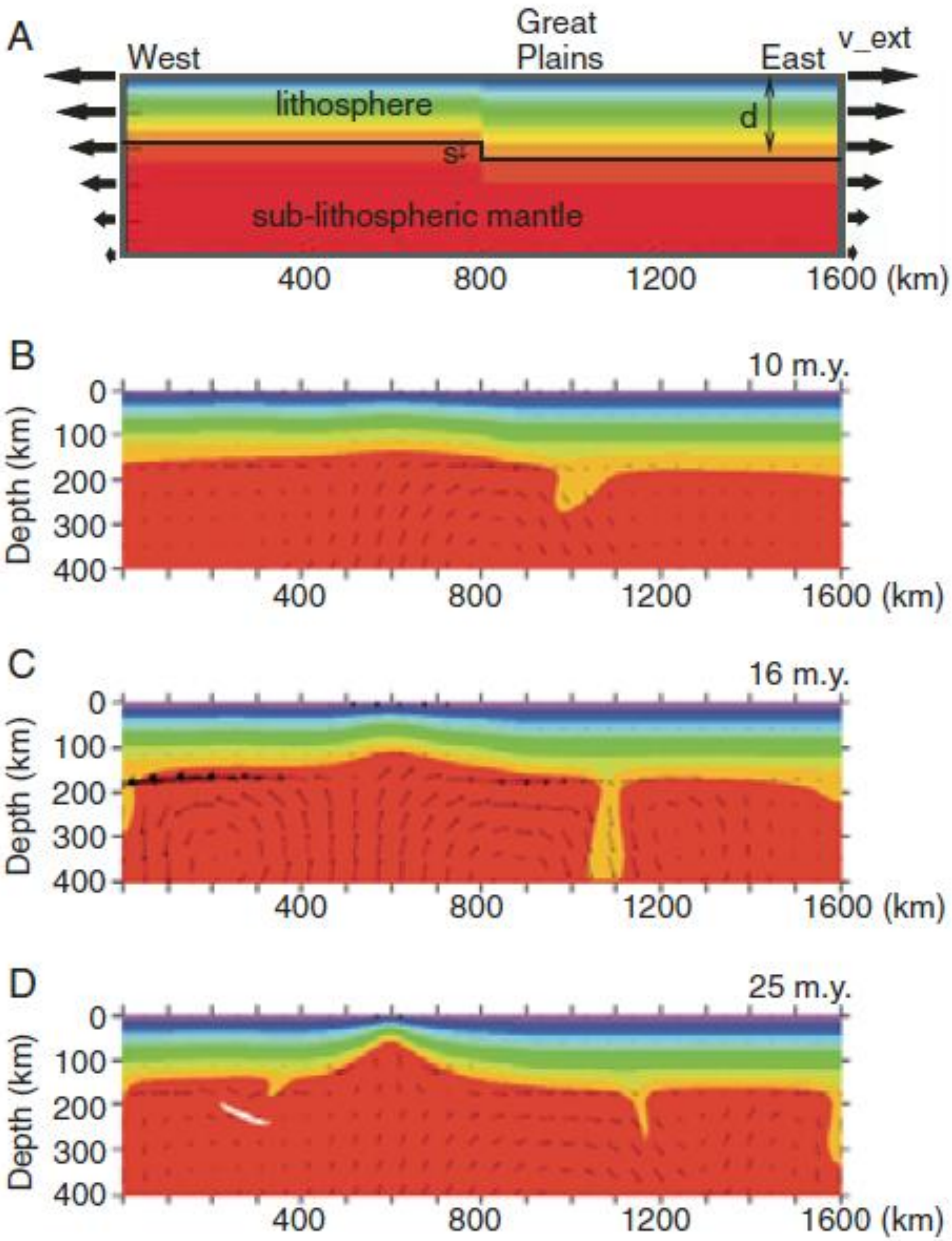

Figure 3. The velocity model A shows the simplified structure of the Rio Grande Rift area to a depth of 400 km where *d* is the depth to the Moho and *s* is the step in thickness from the rift to the Great Plains craton. Large black arrows indicate direction and magnitude of extension. Models B through D illustrate the evolution of the rift over the course of 25 m.y. Small black arrows indicate direction and magnitude of flow (modified from *van Wijk et al*., 2008).

CHAPTER TWO

Methods

The goal of EarthScope's Transportable Array (TA) is to image the structure of the crust and upper mantle beneath the United States in order to understand better its history, composition, and the processes that govern its evolution. However, nominal station spacing for the TA network is 70 km, so, to obtain reliable, high-resolution images of the crust and upper mantle, additional stations must be interspersed between TA stations to reduce station spacing. Beginning in July of 2008, 73 broadband seismometers were deployed through the SIEDCAR project under the temporary network code "XR". SIEDCAR installed one additional station between adjacent TA stations for an approximate station spacing of 35 km (Fig. 4). We used TA (TA) and SIEDCAR (XR) stations in conjunction with a few additional stations to image the upper mantle and crust beneath the array with P and S traveltime tomography. The location of the SIEDCAR deployment was chosen to optimize two-dimensional coverage of the fast seismic anomaly seen in Ristra results. Because earthquakes are most likely to occur on a northwest-southeast trending great circle path that includes the Rio Grande rift, it was expected that the anomaly would be projected along that line, as seen in the Ristra results. SIEDCAR's deployment geometry was determined by the location of the fast anomaly in the mantle beneath Artesia, NM in conjunction with historical seismicity in South America and the Northwest Pacific. The goal was to optimize resolution of the anomaly in three dimensions with respect to expected sources of seismic waves during the 2008 -

2010 deployment duration. In all, 206 stations were analyzed to produce the images presented here, including stations from the XR and TA networks as well as a few stations from the IU, EP, US, and PN networks.

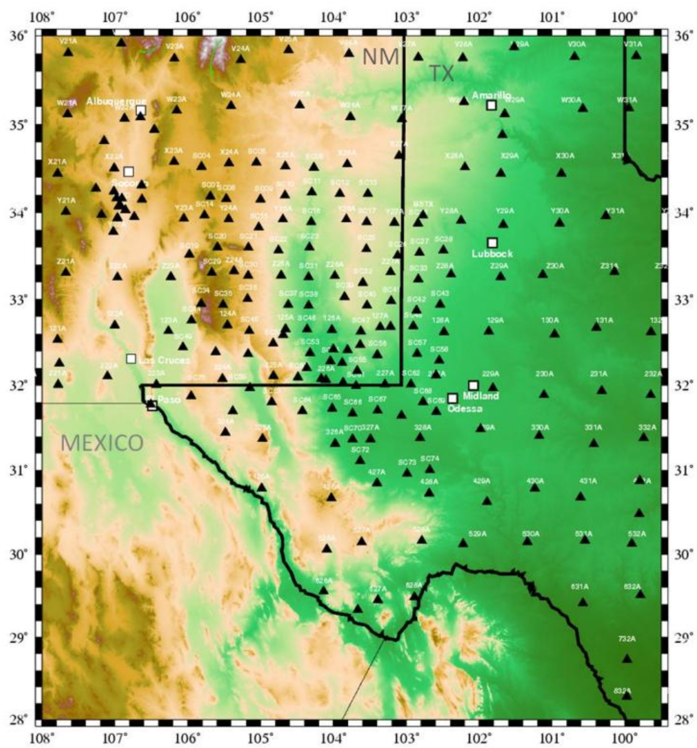

Figure 4. Black triangles denote the locations of seismic stations belonging to six different networks, which recorded P and S wave arrivals used in the tomographic inversion.

All seismographs recorded data at a sample rate of 40 samples/s. Stations recorded many hundreds of events from mid-August 2008 until mid-July 2010 but, in order to use the highest-quality events and obtain relatively even azimuthal distribution, we used only 184 earthquakes for the P-wave model and 98 events for the S-wave model (Fig. 5). We used teleseismic events occurring at epicentral distances of 30° to 90° with a magnitude of 5.0 or greater. We chose the lower threshold for magnitude in order to ensure broad azimuthal coverage.

We used BRTT's Antelope software to organize the database of waveforms and to pick P- and S-wave arrival times. After picking arrivals, we associated each with its respective earthquake. Arrival times and associations were used as input for waveform cross-correlations performed in a MATLAB program coded by Brandon Schmandt (Brandon Schmandt, pers. comm., October 18, 2010). To increase accuracy we cross-correlated waveforms several times for each event. We used a filter of 0.1 Hz for the shear wave correlations and 0.4 Hz for the compressional waves. These cross-correlations produced relative arrival times across the array of 206 stations of the P- or S-wave for each waveform in an event. We then used the resulting delay times as inputs for seismic traveltime tomography. Because our focus is on the model volume directly beneath the array, we assume that lateral heterogeneity outside this volume has no effect on the relative arrival times used in the tomographic inversion (*Rawlinson and Sambridge*, 2003).

Moho topography within the model was addressed by including receiver function results from our UT Austin colleague Yu Xia (Yu Xia, pers. comm., November 11, 2010). Her results provided Moho depths beneath the SIEDCAR array, but not beneath the TA stations at the edges of our model. Because FMTOMO requires each interface to span the entire model region (*Rawlinson*, FMTOMO Instruction Manual), we needed Moho depth values for each velocity node in latitude and longitude. To achieve this, we used the surface algorithm in GMT (Generic Mapping Tools, Wessel and Smith, 1995) to interpolate the Moho structure throughout the rest of the model.

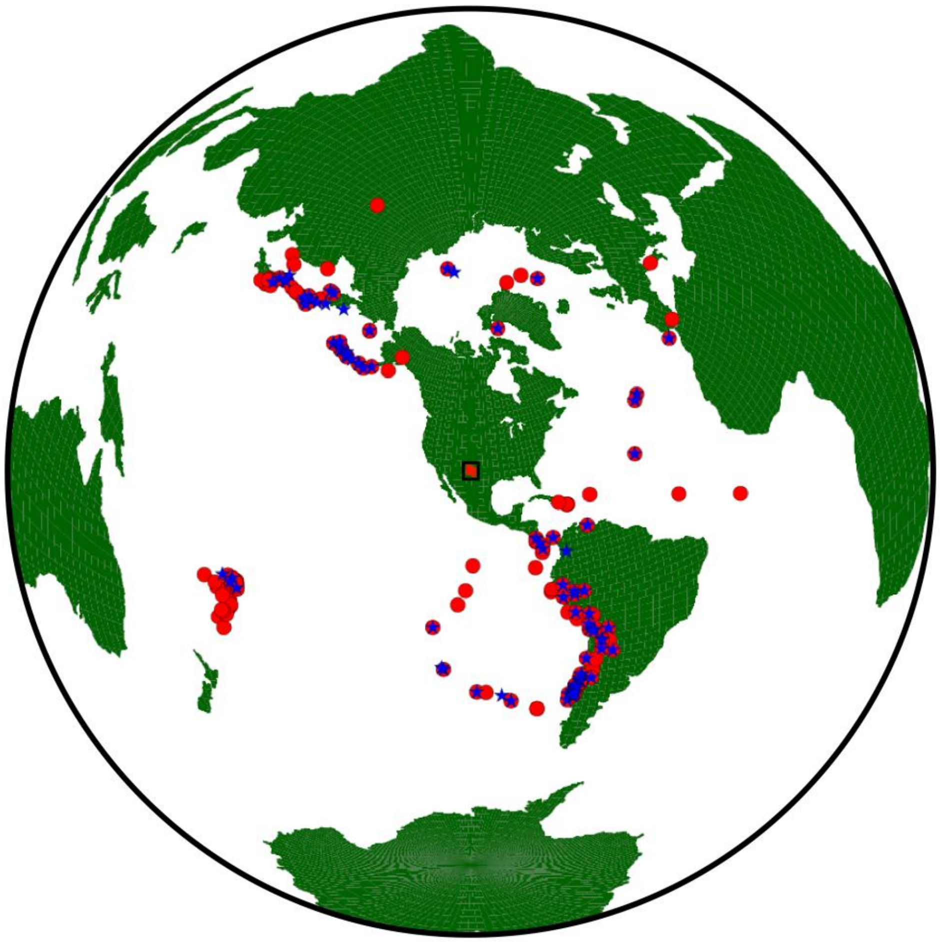

Figure 5. Azimuthal distribution of the 282 earthquakes of magnitude ≥ 5.0 used in the compressional (circles) and shear (stars) wave inversions. All are teleseismic events with distances of 30-90° from the array (center of plot).

The tomographic inversion program we used is called "Fast Marching Tomography" (FMTOMO) (*Rawlinson et al.*, 2006). FMTOMO is an iterative, non-linear method that uses the Fast Marching Method (FMM) – a grid-based eikonal solver – to solve the forward problem of travel time calculation (*Sethian*, 1996, 2001; *Sethian and Popovici*, 1999; *Popovici and Sethian*, 2002; *Rawlinson and Sambridge*, 2003; *de Kool et al.*, 2006). FMM is a finite-difference method which tracks the propagating wavefront to update the traveltime value at each node within the model by solving the eikonal equation

$$|\nabla_{\mathbf{x}} T| = s(\mathbf{x}), \qquad (1)$$

where $\nabla_{\mathbf{x}}$ and T are the gradient operator and traveltime, respectively, and $s(\mathbf{x})$ is slowness (*Rawlinson and Sambridge*, 2004).

The inverse problem is solved by adjusting velocity node values to satisfy data observations. This is achieved with a subspace inversion scheme (*Kennett et al.*, 1988) that minimizes the objective function:

$$S(\mathbf{m}) = (\mathbf{g}(\mathbf{m}) - \mathbf{d}_{\mathrm{obs}})^{\mathrm{T}}\, \mathbf{C}_{\mathrm{d}}^{-1}(\mathbf{g}(\mathbf{m}) - \mathbf{d}_{\mathrm{obs}}) + \varepsilon(\mathbf{m} - \mathbf{m}_0)^{\mathrm{T}}\, \mathbf{C}_{\mathrm{m}}^{-1}(\mathbf{m} - \mathbf{m}_0) + \eta \mathbf{m}^{\mathrm{T}}\mathbf{D}^{\mathrm{T}}\mathbf{D}\mathbf{m} \qquad (2)$$

where $\mathbf{m}$ is the (initially unknown) model parameter vector, $\mathbf{m}_0$ is the reference or starting model, $\mathbf{g}(\mathbf{m})$ represents predicted traveltimes, $\mathbf{d}_{\mathrm{obs}}$ are the observed traveltimes, $\mathbf{C}_{\mathrm{d}}$ is the data covariance matrix, $\mathbf{C}_{\mathrm{m}}$ is the *a priori* model covariance matrix, and $\mathbf{D}$ is the second derivative smoothing operator (*Rawlinson and Kennett*, 2008). Global smoothing is controlled by the factor η while global damping is controlled by ε. Together η and ε are called "regularization parameters". The relative sizes of the regularization parameters create a trade-off between the similarity of the solution to the reference model, the smoothness of the solution, and the differences between the data and solution (*Rawlinson and Kennett*, 2008). Following the inversion, the multi-stage FMM (*de Kool* *et al.*, 2006) updates the path and traveltime information by re-tracing the rays. The iterative process of repeating the forward and inverse steps is continued until the data fit is satisfactory.

By incorporating the Fast Marching Method, FMTOMO holds several advantages compared to alternative schemes (*Rawlinson and Sambridge*, 2004). Most importantly, FMM allows us to compute ray paths and traveltimes in 3D media, accounting for raybending and traveltime perturbations accurately and allowing an iterated non-linear solution to be found. This is an important feature for a study that intends to produce accurate estimates of velocity anomalies' sizes and impedance contrasts. Other methods, most notably methods based on 3D raytracing, can also perform iterated nonlinear inversions but compared to 3D raytracing, FMM is much more computationally stable. Furthermore, FMM combines stability with computational efficiency – a combination lacking in other methods. When grid spacing is reduced, the program's stability allows convergence to the correct high frequency solution while maintaining computational efficiency. Lastly, the method is quite robust - any interface structure (e.g. Moho), velocity, or source location may be found via inversion (APPENDIX A) (*Rawlinson and Kennett*, 2008). One drawback of FMTOMO, however, is that the program cannot perform a joint P and S inversion for V_P/V_S (*Rawlinson*, FMTOMO Instruction Manual). While V_P/V_S values are useful, they are not necessary to achieve our goal. Overall, FMTOMO is well-suited for the purposes of this study.

CHAPTER THREE

Results

Tomographic Models

Both P and S models are defined by 97,196 velocity nodes in three dimensions with velocity node spacing of approximately 24.2 km in depth (to a maximum depth of 500 km), 24.4 km in latitude, and 24.8 km in longitude. The *ak*135 velocity model was used for the reference, or starting, velocity model. Damping (ϵ) and smoothing (η) values were chosen as a trade-off between data variance and model roughness. We used a 20-dimensional subspace scheme on six iterations to solve both P and S inversions. However, in some cases the subspace was reduced by singular value decomposition (SVD) orthogonalization to remove unnecessary basis vectors during the inversion step. Anisotropy, regularization set by smoothing and damping parameters, and unresolved variations in deep mantle and crustal structure may account for some of the data misfit.

A total of 20,485 relative arrival time residuals were inverted using FMTOMO to obtain the final compressional velocity model. Regularization was imposed with $\varepsilon = 5$ and $\eta = 200$. Data variance is reduced by 82% from 1.022 to 0.182 s^2 which corresponds to an RMS reduction from 1011 to 427 ms. The relative arrival time residuals have been reduced to a range of -1.3 to +1.3 s after six iterations (Fig. 6).

Horizontal depth slices show the fast seismic velocity anomaly spans southeastern New Mexico and West Texas (Fig. 7a). The slow velocity material in the west and the fast velocity material in the east correspond to the Rio Grande rift and the Great Plains craton, respectively. The slow velocity material beneath the Texas panhandle

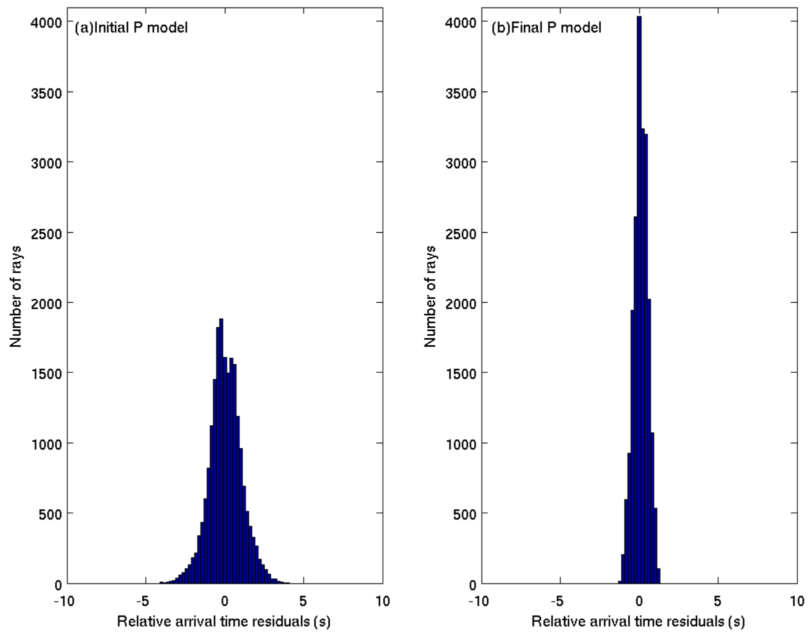

Figure 6. Histograms showing the distribution of relative arrival time residuals of the compressional model in (a) the starting model and (b) the final model.

corresponds to the Southern Oklahoma Aulacogen, a failed rift arm that dates to ~550 Ma (*Ham et al.*, 1965; *Lambert et al.*, 1988). E-W cross-sections show a clear disconnect from fast craton material (Fig. 7c). The N-S cross-sections suggest that the anomaly deepens northward (Fig. 7b).

A total of 9717 residuals were used in the shear wave inversion. For this model, a regularization of $\varepsilon = 1$ and $\eta = 200$ was imposed. Data variance here is reduced by 74% from 1.945 to 0.505 s^2 which corresponds to an RMS reduction from 1395 to 711 ms. Residuals of the shear model have been reduced to a range of -1.5 to 2.1 s after six iterations of FMTOMO (Fig.8).

Depth sections of our S model show the anomaly to be broken apart or discontinuous (Fig. 9). As in the P model, E-W cross-sections of the S model show the

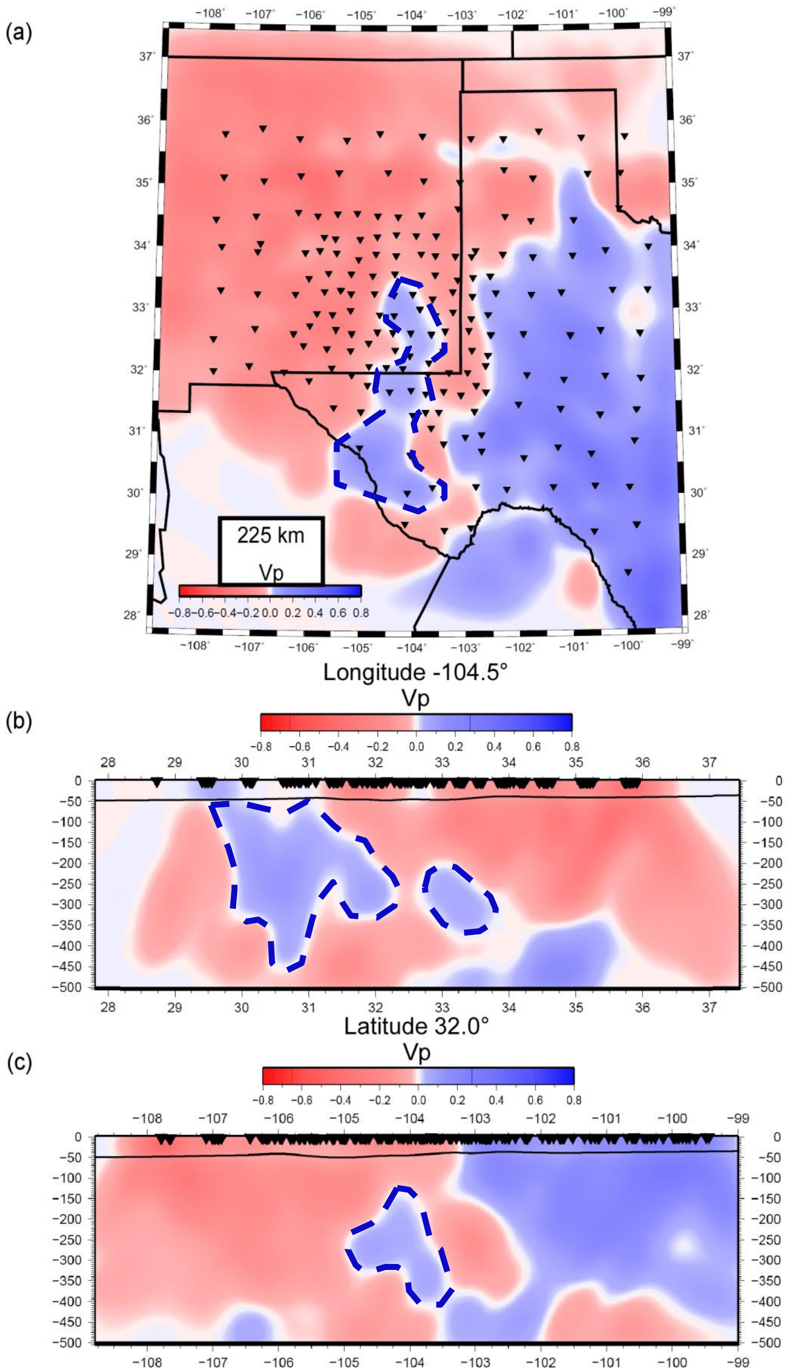

Figure 7. (a) Horizontal section through the three-dimensional compressional velocity model at 225 km depth; (b) longitudinal cross-section through -104.5°; (c) latitudinal cross-section through 32.0°. The fast seismic anomaly is outlined by the dashed line.

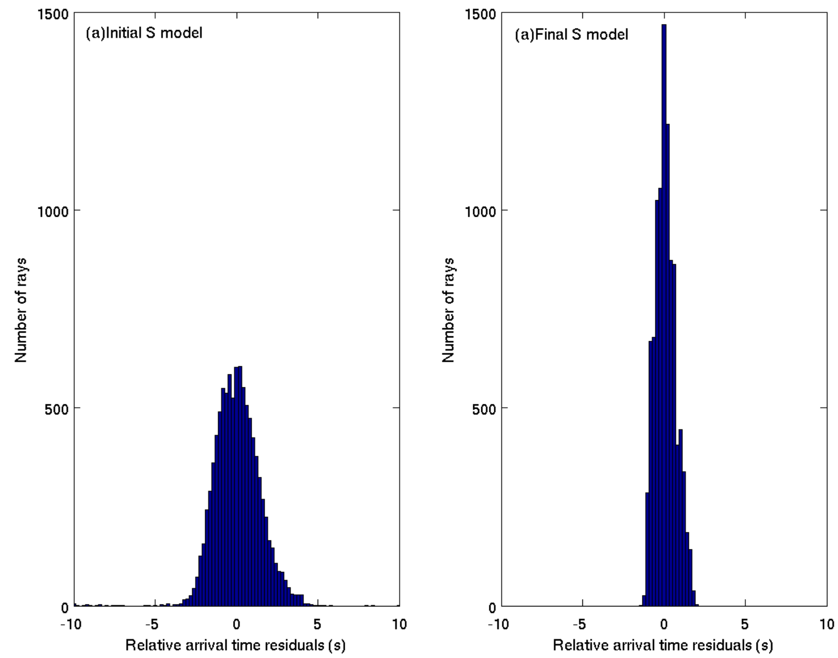

Figure 8. Histograms showing the distribution of relative arrival time residuals of the shear model in (a) the starting model and (b) the final model.

anomaly is mostly disconnected from the craton. N-S cross-sections show the anomaly to be quite laterally heterogeneous and deepening northward.

Our results differ from the La Ristra results in that our models show that the anomaly is larger and extends further southward than we originally thought. Additionally, La Ristra results suggest the anomaly lies beneath the Great Plains craton, while our results show the anomaly adjacent to the craton. Our models show the bulk of the anomaly lies beneath west Texas and southeastern New Mexico as a somewhat discontinuous structure. Both models show the anomaly extending from just below the Moho in the southwest to depths of at least 500 km in the northeastern portion. The anomaly appears clearly disconnected from the craton at 225 km depth in the

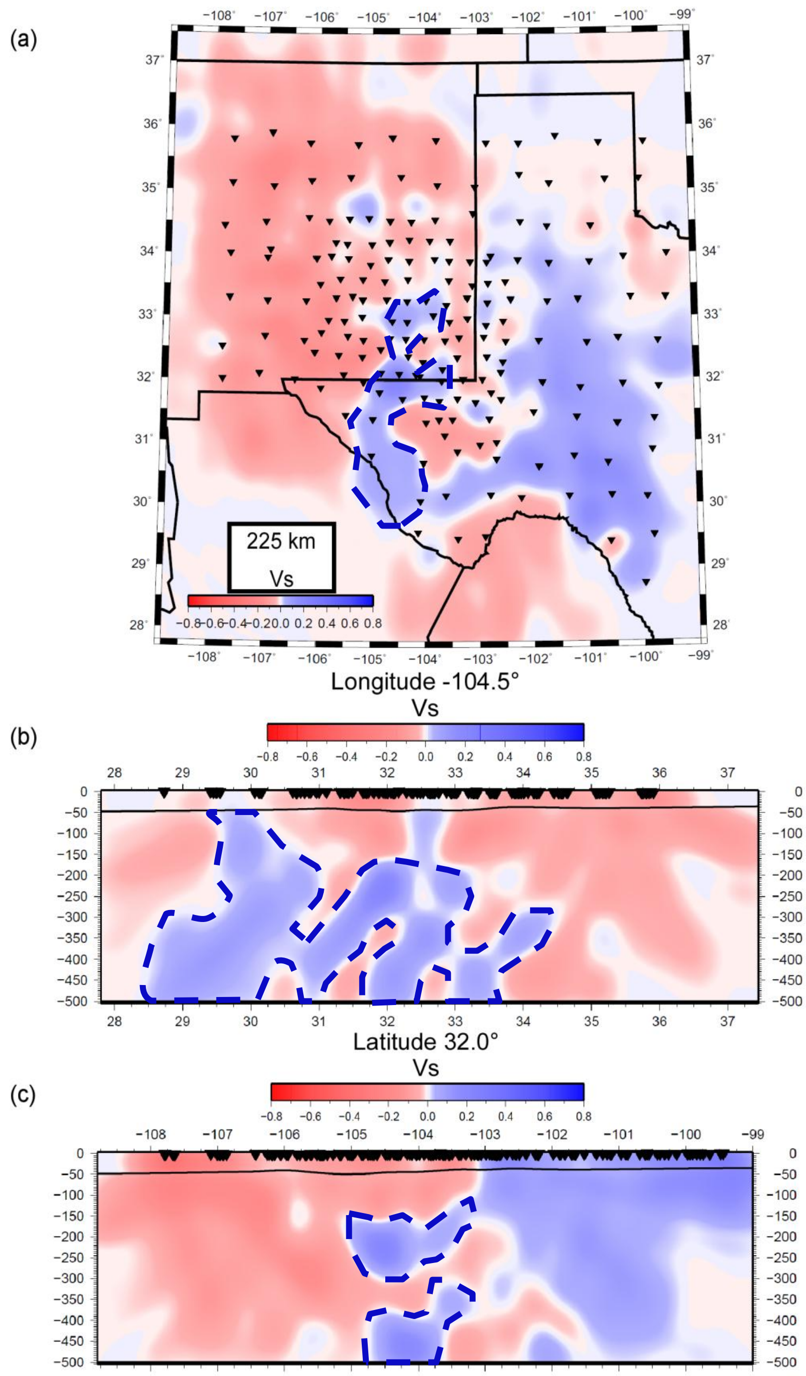

Figure 9. (a) Horizontal section through the three-dimensional shear velocity model at 225 km depth with fast anomaly outlined in dark blue dashed line; (b) longitudinal cross-section through -104.5°; (c) latitudinal cross-section through 32.0°. The fast seismic anomaly is outlined by the dashed line.

compressional velocity model (Fig. 7), but appears to be still connected at some locations at shallower depths (APPENDICES B-D). This is also apparent in the shear velocity model (APPENDICES E-G). While our model shows the anomaly extending into Chihuahua, Mexico, we are unable to say to what extent as our data covereage was only within the United States.

Resolution Analysis

Synthetic resolution tests evaluate the constraints of the dataset on the model parameters. In other words, we can see where our solution model is well constrained and where it is poorly constrained on the basis of adequate ray-path coverage and arrival time uncertainty (*Rawlinson and Kennett,* 2008). The resolution test that we use here is called the "checkerboard test" (*Hearn and Clayton*, 1986; *Glahn and Granet*, 1993; *Graeber and Asch*, 1999; *Rawlinson and Sambridge*, 2003; *Rawlinson and Kennett*, 2008). The starting model is comprised of a checkerboard pattern of alternating fast and slow anomalies in three dimensions. Using the same source-receiver configuration and the same phase as the observed data, a checkerboard structure is created by solving the forward problem with the checkerboard pattern turned on. The starting model is created with the checkerboard pattern turned off. The dataset is then used in conjunction with the reference model to solve the inverse problem. The solution model should recover the checkerboard pattern in areas that are well resolved.

To test the resolution, we ran a series of checkerboard tests, each with maximum amplitude ±0.5 km/s, with varying checkerboard sizes. The size of the checkerboard indicates the scale of resolution achieved within the model. Our checkerboard tests range in size from ~48 km to ~144 km in each dimension for both the P (Fig. 10) and S (Fig.

12) models. Beneath the SIEDCAR array (~35 km station spacing), small and large-scale resolution was achieved up to 500 km depth in both P (Fig. 11) and S (Fig. 13) models. Small-scale resolution depth decreased with distance from the center of the array. Both models show smearing in a northeast-southwest trend (Fig. 11a, Fig. 13a), possibly due to the lack of earthquake data occurring along that trend (Fig. 5).

Errors in our results can be attributed to several sources. The selection of the first P and S phase arrival time is subject to some error, albeit only fractions of a second. Where the BRTT Antelope software's auto detection failed, clear first arrivals were hand-picked. Errors in selection can introduce error into the succeeding cross-correlation and inversion steps. However, such small errors are not likely to produce significant changes in the final result. As seen in Figure 5, the majority of the earthquakes used for the inversion originate to the northwest and to the southeast of the array. The dearth of ray-paths coming from the north-northeast and southwest, especially for the S model, creates a bias which contributes to smearing in our results.

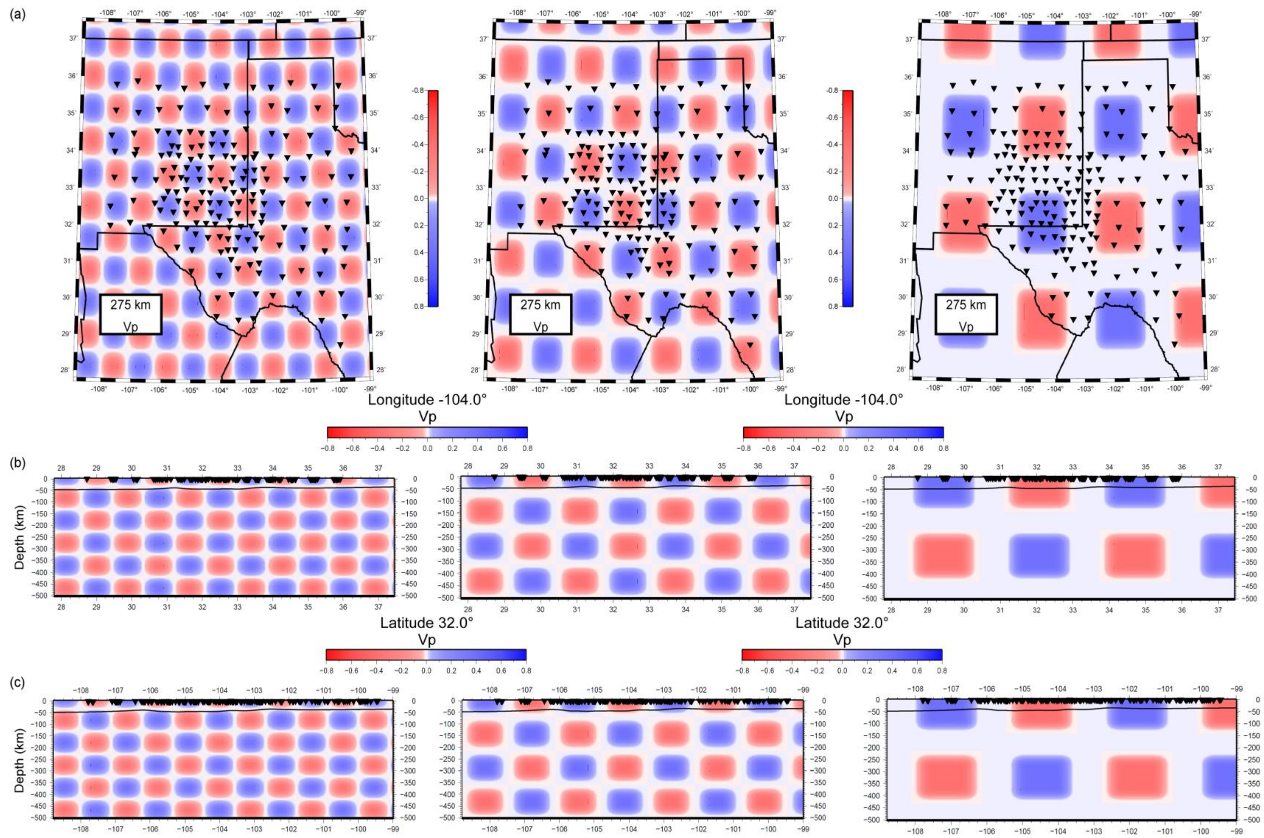

Figure 10. Reference checkerboard model for resolution test of the compressional model with checkerboard sizes of two velocity nodes or ~48 km in the first column, three velocity nodes or ~72 km in the center column, and six velocity nodes or ~144 km in the far right column. Each column shows (a) a depth slice at 275 km, (b) a longitudinal slice at -104.0°, and (c) a latitudinal slice at 32.0°.

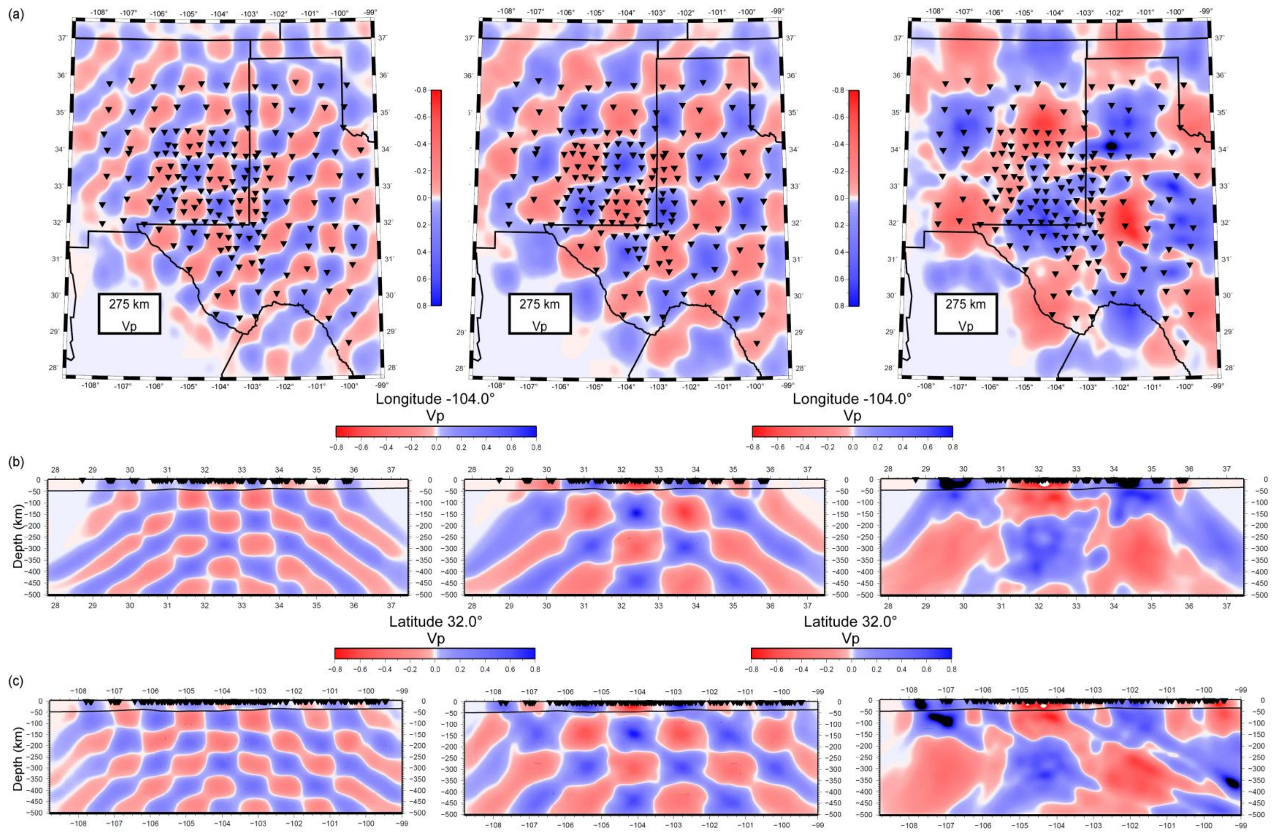

Figure 11. Recovered checkerboards for the compressional model with checkerboard sizes of two velocity nodes or ~48 km in the first column, three velocity nodes or ~72 km in the center column, and six velocity nodes or ~144 km in the far right column. Each column shows (a) a depth slice at 275 km, (b) a longitudinal slice at -104.0°, and (c) a latitudinal slice at 32.0°.

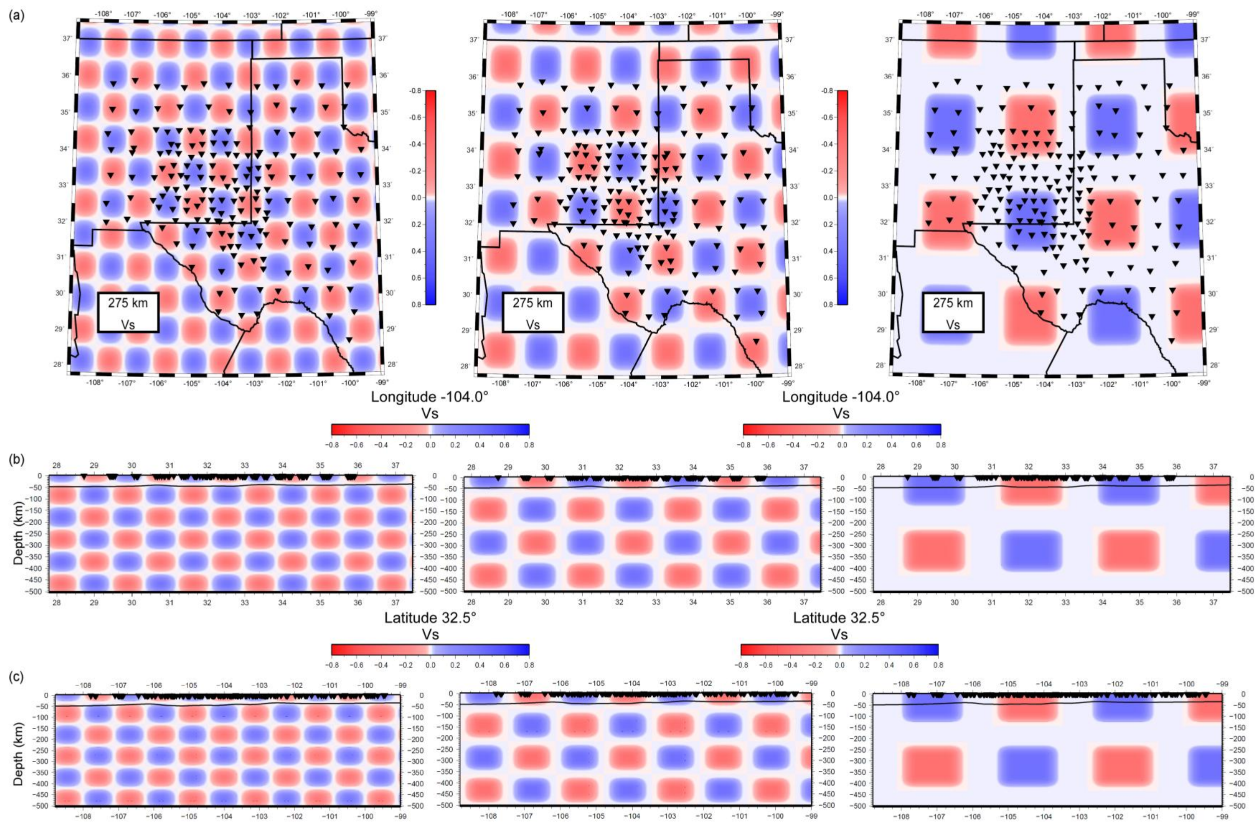

Figure 12. Reference checkerboard model for resolution test of the shear model with checkerboard sizes of two velocity nodes or ~48 km in the first column, three velocity nodes or ~72 km in the center column, and six velocity nodes or ~144 km in the far right column. Each column shows (a) a depth slice at 275 km, (b) a longitudinal slice at -104.0°, and (c) a latitudinal slice at 32.5°.

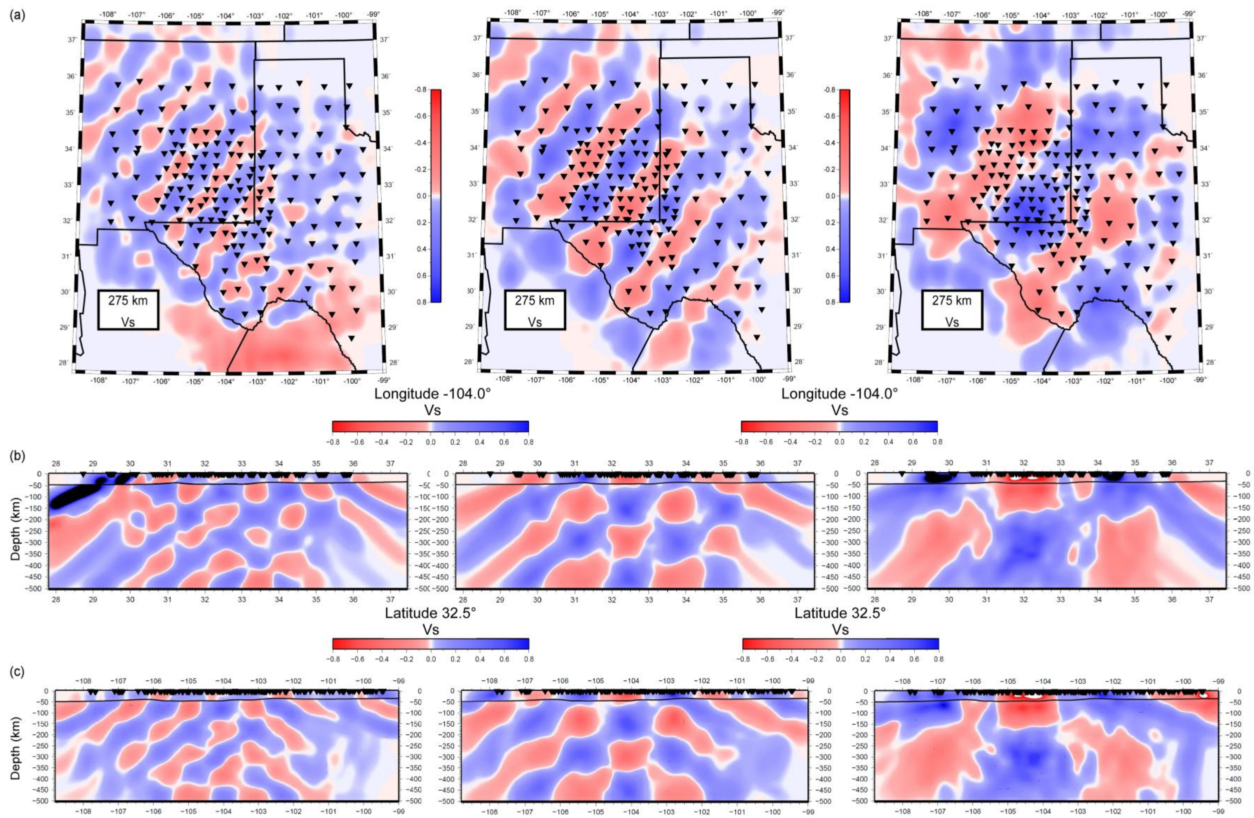

Figure 13. Recovered checkerboards for the shear model with checkerboard sizes of two velocity nodes or ~48 km in the first column, three velocity nodes or ~72 km in the center column, and six velocity nodes or ~144 km in the far right column. Each column shows (a) a depth slice at 275 km, (b) a longitudinal slice at -104.0°, and (c) a latitudinal slice at 32.5°.

CHAPTER FOUR

Discussion

By comparing our tomographic models to those from the Ristra transect presented by *Gao et al.* (2004), we can confirm that the fast seismic structure in our inversions is the same as that seen in the Ristra results (Fig. 14). Due to the structure of the seismic array, the dataset, and the issue of non-uniqueness, our models differ in some ways from those of the Ristra transect. The slow material beneath the Rio Grande rift is much more prominent and extends to greater depths in our results, and the geometry of the fast anomaly is different. However, the fast anomaly is in the same general location and is more prominent in the shear velocity model for both the Ristra and SIEDCAR models. The large body of fast velocity material between -104° and -105° above 200 km in the Ristra images (Fig. 14a) is not apparent in the SIEDCAR images (Fig. 14b). This feature is most likely representative of the Great Plains craton and is probably an off-line projection. The absence of this feature above the anomaly in our model leads us to question the hypothesis of edge-driven convection as a driving mechanism. In the *van Wijk et al.* (2008) model of edge-driven convection, the anomaly lies beneath the craton several hundreds of kilometers from the rift axis. This is not the case in our model; the anomaly is only ~100 km from the rift axis and is adjacent to rather than beneath the craton. Therefore, we must explore other possible origins for the anomaly.

Due to its greater density, the continental mantle lithosphere is negatively buoyant with respect to the asthenosphere (*Bird,* 1978; *Molnar and Gray,* 1979). Therefore, if the mantle lithosphere detached from the overlying crust it could be expected to sink into the

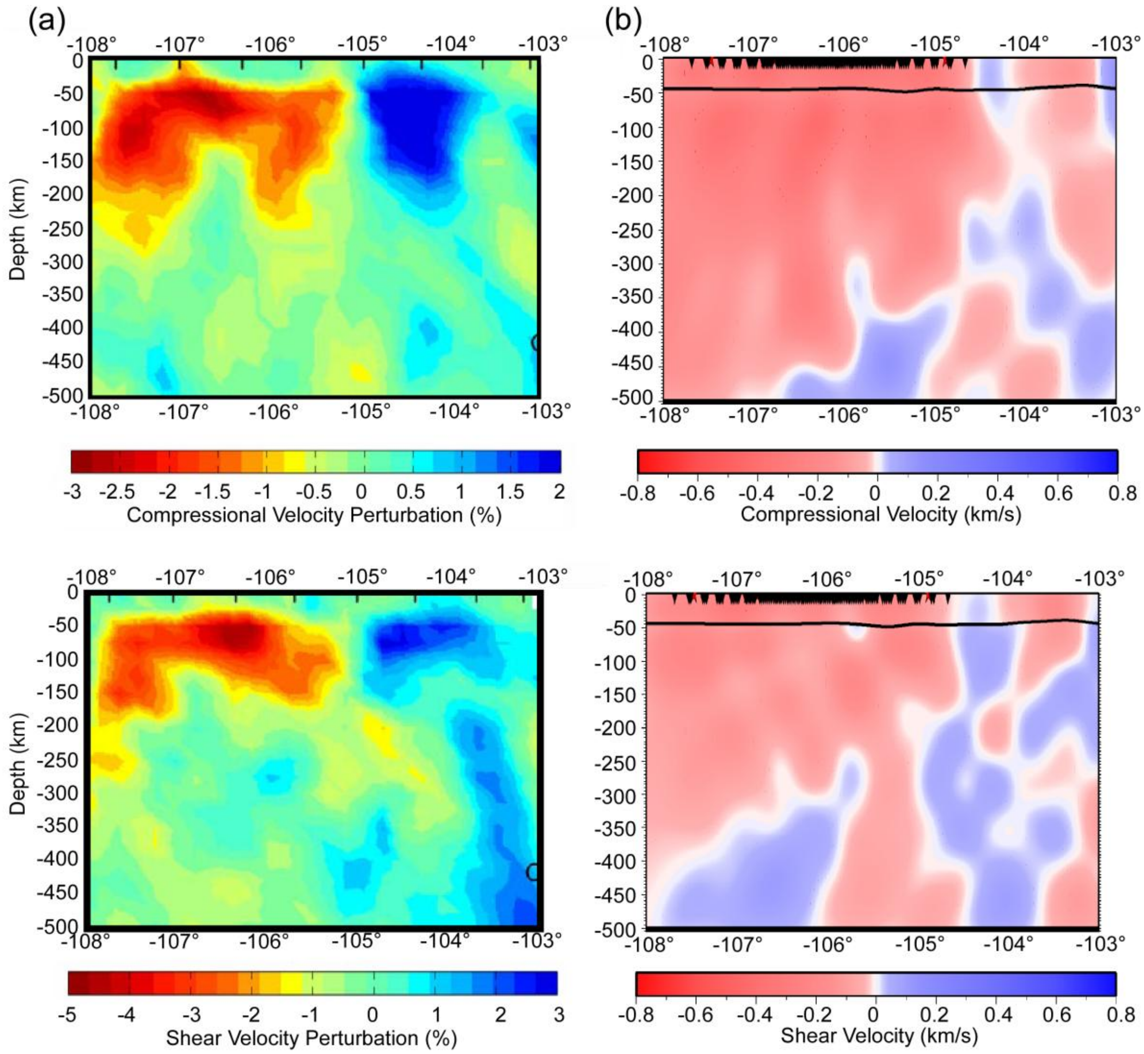

Figure 14. (a) Tomographic results from the La Ristra array (Gao et al., 2004), and (b) a slice corresponding to the La Ristra transect taken from tomographic results of the SIEDCAR array. Top images shows compressional velocity and bottom images show shear velocity.

mantle (*Bird*, 1978, 1979; *Molnar and Gray,* 1979; *Bird and Baumgardner*, 1981). One potential mechanism for detachment is the convective removal of lithospheric root edges (*Doin et al.,* 1997; *Morency et al.,* 2002). *Morency et al.* (2002) show how cool, dense lithospheric roots are shortened over time by the erosion and convective removal of their edges. In our case, the lateral temperature and density heterogeneities from the thinned rift to the thicker craton create an edge-driven convection process that may drive lithospheric root shortening or removal (Fig. 15). *Morency et al.* (2002) model the entrainment of the craton edge into the downwelling convection cell as opposed to a convective drip beneath the craton as described by *van Wijk et al.* (2008). When considering convective lithospheric erosion as a driving mechanism in our model it is important to note that in the northern part of the rift, the amount of total extension decreases (*Cordell*, 1978) and the area of high heat flow narrows (*Decker and Smithson*, 1975; *Reiter et al.*, 1975, 1978, 1979; *Smith and Jones*, 1979; *Swanberg*, 1979; *Clarkson and Reiter*, 1984; *Decker et al.*, 1984 1988). The shorter length of extension and narrower band of high heat flow imply a smaller convection cell, if any exists at all. It is possible that the smaller amount of extension in the north did not promote lithospheric destabilization, and therefore would not produce a detached fast seismic velocity anomaly in the narrower, northern portion of the rift. This would explain why our models show

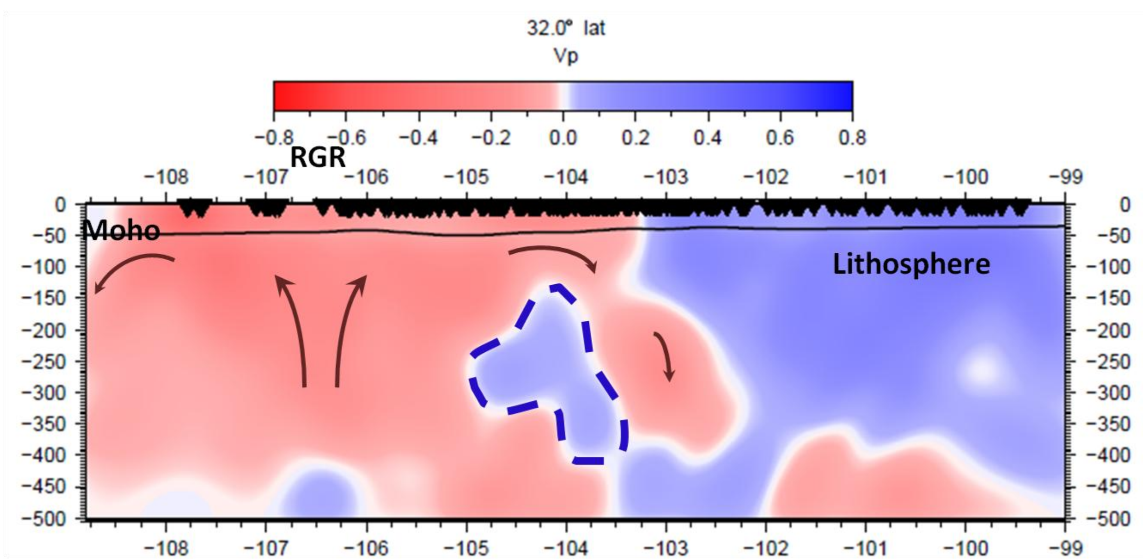

Figure 15. Illustration of convective lithospheric erosion as a driving mechanism for the fast seismic velocity anomaly, outlined by the dashed line. Arrows indicate convective motion, particularly of asthenospheric material.

the anomaly extending only to ~34°N and not farther north. Another possibility is that the detached anomaly has an effect on tectonic and extensional processes such that the southern portion of the rift experienced greater extension than the northern portion, or vice versa: greater extension is the cause for the lithospheric erosion and detachment in the south. Because the timing of the origin of the anomaly is uncertain, it is unclear whether mantle structure affected extension rates, varying rates of extension affected mantle processes, or an outside variable affected both extension rates and mantle processes. In any case, something about the geodynamic process differs between the southern and northern parts of the Rio Grande rift.

Both uplift and magmatism are expected in the presence of lithospheric removal (*Bird*, 1979). There has been approximately 1 km of uplift in the southern Rockies within the last 13 m.y. (*Axelrod and Bailey*, 1976; *Morgan et al*., 1986; *Eaton*, 1986), however because the anomaly does not extend as far north as the southern Rockies, we cannot associate this uplift with lithospheric removal. Uplift within the Sandia and Sacramento Mountains is attributed to flexural uplift along the eastern rift flank (*House et al.,* 2003; *Brown and Phillips,* 1999). The mechanisms driving this flexural uplift are uncertain, though *Brown and Phillips* (1999) suggest that the Sacramento Mountain uplift may be driven by mantle processes such as small-scale convection. With the Sacramento uplift began the Pecos River valley depression less than 12 Ma (*Brown and Phillips,* 1999). The valley correlates spatially to a large portion of the anomaly (Fig. 16). We consider that the sinking eroded lithosphere may be pulling the crust creating a topographic depression here (APPENDIX I). Such a mechanism would also contribute to the flexural uplift of the eastern flank of the rift. However, the depression is also related

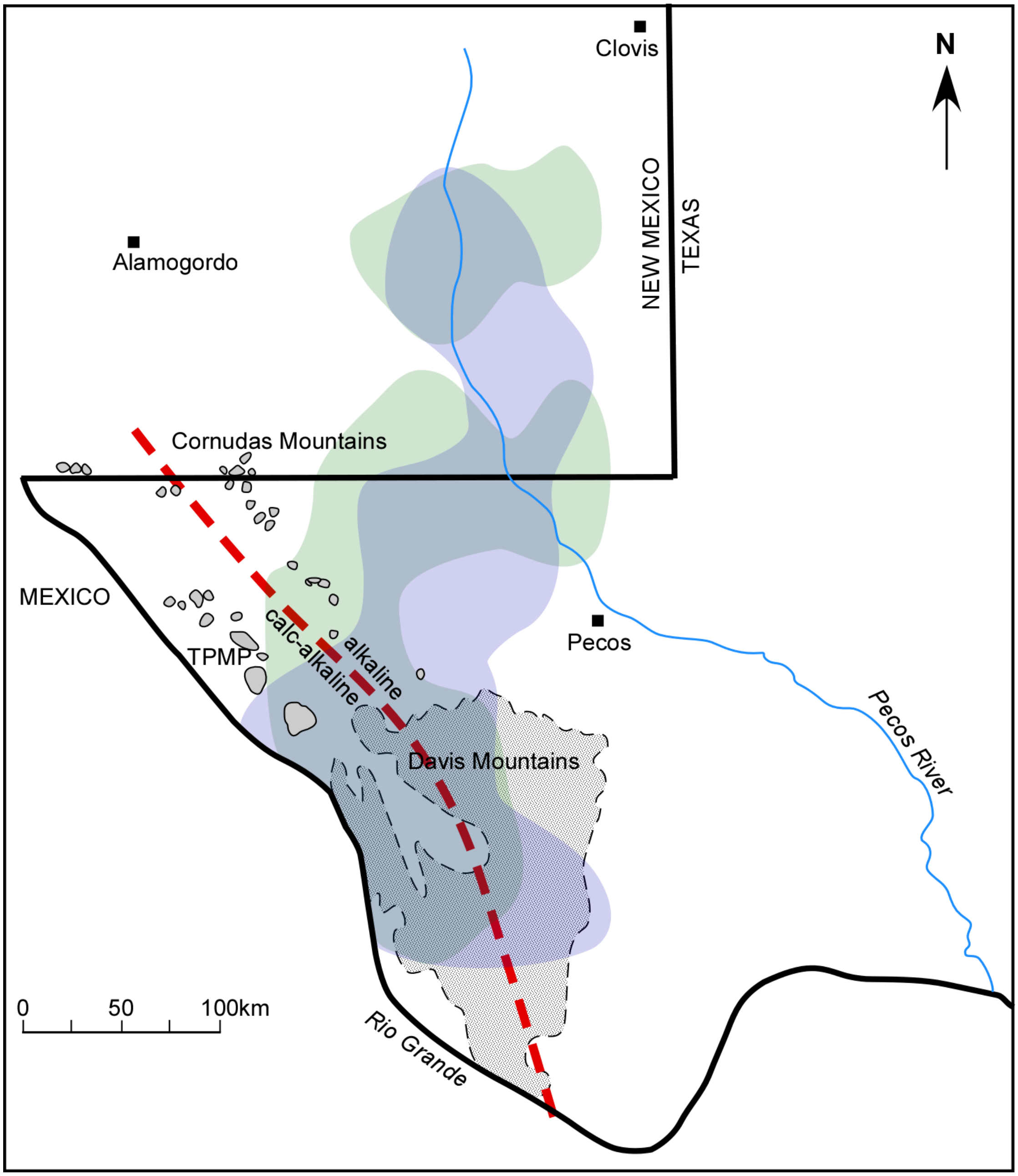

Figure 16. Blue and green shaded areas are projections of the P and S fast seismic anomaly, respectively, at 225 km depth. The location of the anomaly is coincident with the southern Cornudas Mountains and Trans-Pecos Magmatic Province (TPMP), especially the Davis Mountains. The dashed line (*Barker*, 1987) separates the alkalic rocks to the east from the calc-alkalic magmatics to the west (modified from *McLemore et al*., 1996).

to stream erosion (*Thomas,* 1972). While erosion has an obvious role in the valley's evolution, the possibility of downwarping of the Earth's surface as a dynamic effect of a "drip" in the mantle has not been modeled in the area and remains unclear.

There are several magmatic intrusions in southeastern New Mexico and west Texas that are contemporaneous with Rio Grande rift activity. The Trans-Pecos magmatic field and the southern Cornudas peaks correlate with the location of the fast seismic anomaly (Fig. 15) (*McLemore et al.,* 1996). These peaks are distributed across the surface above the anomaly and range in age from 48 to 17 Ma (*Price et al.,* 1987; *McLemore et al.,* 1996). Furthermore, there is a clear separation between calc-alkalic and alkalic signatures within west Texas (Fig. 15) which may indicate a shift from a lithospheric source for the calc-alkaline rocks to an asthenospheric source for the alkaline rocks (*Barker,* 1987; *McLemore et al.,* 1996). This would be expected if the lithosphere were removed and asthenosphere replaced it during lithospheric erosion. Additionally, there are igneous dikes just east of the Guadalupe Mountains that are believed to have originated in the Oligocene (*Calzia and Hiss,* 1978).

To improve the modeling of the upper mantle and lower crust in this area, future studies should include joint P and S tomographic inversions on these data. Better resolution may be obtained by including the PKP phase in the tomographic inversion. This would allow the ray paths to arrive at receivers at a nearly vertical angle to obtain higher lateral resolution. In order to clarify whether this fast seismic velocity anomaly is the signature of sinking, eroded lithosphere, additional studies must be conducted. In particular, the quantitative constraints on the geometry and velocity contrast obtained through this study should be used to create three-dimensional geodynamic models of the area. Geodynamic models will be useful in determining whether convective lithospheric erosion is occurring beneath the Great Plains in addition to exploring and illustrating the possibilities of associations between mantle and surface processes.

CHAPTER FIVE

Conclusions

The three dimensional P and S tomographic models presented here allow us to confirm the fast seismic anomaly seen in the La Ristra results but also to constrain its lateral and vertical extent. Our results show that the anomaly extends slightly further to the north and much further south than could be seen from the 2D Ristra result. By comparing our models to the geodynamic models of *van Wijk et al.* (2008) we find discrepancies between the location and geometry of the anomaly found in our results and their geodynamic model. Because of these discrepancies, we believe that edge-driven convection is not the driving mechanism behind the fast seismic velocity anomaly. The geometry and location of the anomaly as seen in our models suggests convective lithospheric removal, as described by *Morency et al.* (2002). The detachment of the anomaly from the Great Plains craton and the fact that it is adjacent to, rather than beneath, the craton edge implies that the lithosphere is being removed or eroded from the craton edge. Regional uplift and magmatism, which are expected to accompany lithospheric erosion, are evident on the surface above the anomaly and are contemporaneous with regional extension. Extension within the southern portion of the Rio Grande rift is vastly different from that of the northern portion. While it remains unclear exactly why the rift changes so much from north to south, we show that this difference is apparent not only on the surface but also within the mantle.

To clarify the driving mechanism of the anomaly, and to understand better the association of surface and mantle processes, three dimensional geodynamic models should be created using the constraints that we have found. Resolution of the models can be enhanced by adding the PKP phase to the tomographic inversion, and Vp/Vs values can be analyzed by performing a joint P and S inversion. Finally, a detailed petrological analysis of those intrusions that correlate with the location of the anomaly may provide a clearer history of their evolution.

APPENDICES

APPENDIX A

FMTOMO Input File Examples

```
cccccccccccccccccccccccccccccccccccccccccccccccccccccc^M
c Specify number of layers (= number of interfaces -1)^M
cccccccccccccccccccccccccccccccccccccccccccccccccccccc^M
2                       c: Number of layers in model^M
1                       c: Number of velocity grid types (1 or 2)^M
0.2                     c: Pinchout distance (km) (>=0.0)^M
vgrids.in               c: Output velocity grid file^M
interfaces.in           c: Output interface grid file^M
-12325                  c: Seed for random number generation (int)^M
0.20                    c: Minimum permitted velocity (km/s)^M
cccccccccccccccccccccccccccccccccccccccccccccccccccccc^M
c Set 3-D grid size and location. Note that all layer^M
c velocity grids have the same spatial dimension, but can^M
c have different node densities. Interface grids have the^M
c same node distribution.^M
cccccccccccccccccccccccccccccccccccccccccccccccccccccc^M
2.50    -505.50         c: Radial range (top-bottom) of grid (km)^M
37.45    27.8            c: Latitudinal range (N-S) of grid (degrees)^M
-108.8  -99.0            c: Longitudinal range (E-W) of grid (degrees)^M
6371.0                 c: Earth radius^M
ccccccccccccccccccccccccccccccccccccccccccccccccccccccc^M
c Set up propagation grid file^M
ccccccccccccccccccccccccccccccccccccccccccccccccccccccc^M
propgrid.in             c: Name of propagation grid file^M
75   75    75           c: Number of points in rad lat, long^M
5     5                 c: Refine factor & no. of local cells^M
0.01                    c: Cushion factor for prop grid (<<1)^M
ccccccccccccccccccccccccccccccccccccccccccccccccccccccc^M
ccccccccccccccccccccccccccccccccccccccccccccccccccccccc^M
c First, set up the velocity grids^M
ccccccccccccccccccccccccccccccccccccccccccccccccccccccc^M
ccccccccccccccccccccccccccccccccccccccccccccccccccccccc^M
c Set velocity grid values for layer 1^M
ccccccccccccccccccccccccccccccccccccccccccccccccccccccc^M
22        12            c: Number of radial grid points (type 1 & 2)^M
45        2             c: Number of grid points in theta (N-S)^M
45        12            c: Number of grid points in phi (E-W)^M
0                       c: Use model (0) or constant gradient (1)^M
P                       c: Use P or S velocity model^M
ak135true.vel           c: Velocity model (option 0)^M
1                       c: Dimension of velocity model (1=1-D,3=3-D)^M
6.1       4.0           c: Velocity at origin (km/s) (option 1)^M
9.0       7.0           c: Velocity at maximum depth (km/s) (option 1)^M
```

Figure A.1. FMTOMO file *grid3dg.in*; the file is modified by hand to create the model space used in the tomographic inversion.

```
cccccccccccccccccccccccccccccccccccccccccccccccccccccccccccccccccc
c Input file for generating source and receiver files
c for use by 3D FMM code. Will also generate traveltime
c file if required.
cccccccccccccccccccccccccccccccccccccccccccccccccccccccccccccccccc
sources.in                  c: Output source file
receivers.in                c: Output receiver file
sourcederivs.in             c: Output source derivative file
picks/                      c: Directory containing input receiver files
1                           c: Number of input source files
1                           c: Extract traveltimes (0=no, 1=yes)
otimes.dat                  c: File containing extracted traveltimes
cccccccccccccccccccccccccccccccccccccccccccccccccccccccccccccccccc
c Second input source file and associated path information
cccccccccccccccccccccccccccccccccccccccccccccccccccccccccccccccccc
telePP                       c: Input source file
1                           c: Local (0) or teleseismic sources (1)
0                           c: Compute source derivatives (0=no, 1=yes)
1                           c: Number of paths from these sources
2                           c: Number of path segments for path 1
c: Path sequence information plus velocity fields below
3 2  2 1
1    1
```

Figure A.2. FMTOMO file *obsdata.in*; this input file is modified by hand to add source files, to indicate whether local or teleseismic events are being used, and to describe the ray paths.

```
        184
          1
P
   13.00000      -1.020000      -21.84300
          1
          2
          3            2            2            1
          1            1
          1
P
   8.000000      -15.08700      -173.4760
          1
          2
          3            2            2            1
          1            1
          1
P
   154.0000      -7.641000      -74.37700
          1
          2
          3            2            2            1
          1            1
          1
P
   171.1000      -25.38700      -177.6360
```

Figure A.3. FMTOMO file *sources.in*; this file is created by running *obsdata* and described the location and ray path of each source used in the inversion.

```
     20485
  1.652000      32.53000      -107.7900
           1
           1
           1
  1.436000      34.07000      -106.9200
           1
           1
           1
  2.229000      32.93694      -105.5153
           1
           1
           1
  1.667000      33.59750      -105.1655
           1
           1
           1
  1.641000      33.00533      -105.1800
           1
           1
           1
  1.473000      33.83083      -105.0255
           1
           1
           1
```

Figure A.4. FMTOMO file *receivers.in*; this file is created by running *obsdata* and describes the location of each receiver in the array for every event used.

```
20485
    1          1          1          0   1.945900      0.1000000
    2          1          1          0  0.2277000      0.1000000
    3          1          1          0  0.5974000      0.1000000
    4          1          1          0  0.6762000      0.1000000
    5          1          1          0  0.5368000      0.1000000
    6          1          1          0  0.3762000      0.1000000
    7          1          1          0  0.3944000      0.1000000
    8          1          1          0  9.4400004E-02  0.1000000
    9          1          1          0  4.4399999E-02  0.1000000
   10          1          1          0  0.5353000      0.1000000
   11          1          1          0  0.5808000      0.1000000
   12          1          1          0  0.7141000      0.1000000
   13          1          1          0  0.2929000      0.1000000
   14          1          1          0  0.3929000      0.1000000
   15          1          1          0 -5.5599999E-02  0.1000000
   16          1          1          0  0.8853000      0.1000000
   17          1          1          0  0.1626000      0.1000000
   18          1          1          0  0.3247000      0.1000000
   19          1          1          0 -0.2238000      0.1000000
   20          1          1          0 -0.2495000      0.1000000
   21          1          1          0 -0.2329000      0.1000000
   22          1          1          0 -0.5556000      0.1000000
   23          1          1          0 -0.8829000      0.1000000
   24          1          1          0 -0.8298000      0.1000000
```

Figure A.5. FMTOMO file *otimes.dat*; this input file is created by running *obsdata* and lists observed relative arrival time residuals (in seconds) in the fourth column along with its uncertainty in the fifth column for each source-receiver pair.

```
184
1 1 pa.P_000001.evt
1 1 pa.P_000002.evt
1 1 pa.P_000003.evt
1 1 pa.P_000005.evt
1 1 pa.P_000006.evt
1 1 pa.P_000007.evt
1 1 pa.P_000008.evt
1 1 pa.P_000009.evt
1 1 pa.P_000012.evt
1 1 pa.P_000013.evt
1 1 pa.P_000014.evt
1 1 pa.P_000015.evt
1 1 pa.P_000016.evt
1 1 pa.P_000017.evt
1 1 pa.P_000018.evt
1 1 pa.P_000019.evt
1 1 pa.P_000020.evt
1 1 pa.P_000021.evt
1 1 pa.P_000023.evt
1 1 pa.P_000024.evt
1 1 pa.P_000025.evt
1 1 pa.P_000026.evt
1 1 pa.P_000027.evt
```

Figure A.6. FMTOMO input source file; this file contains the complete list of event files to be used in the inversion with the total number of events listed on the first line.

```
   86
-25.71200  -66.61700   10.0
P
  31.89000  -101.11000 0.742   -1.1069  0.10
  31.31000  -100.43000 0.615   -1.4885  0.10
  31.38000   -99.74000 0.513   -1.6130  0.10
  30.62000  -101.89000 0.804   -0.8446  0.10
  30.12000  -102.22000 0.764   -0.8145  0.10
  30.15000  -101.34000 0.636   -1.2354  0.10
  30.13000   -99.90000 0.703   -1.7293  0.10
  29.41000  -100.58000 0.344   -2.3752  0.10
  29.51000   -99.79000 0.420   -2.1671  0.10
  28.73000   -99.97000 0.178   -2.5773  0.10
  32.62000   -99.64000 0.502   -0.9166  0.10
  30.96110  -102.98746 0.887   -0.2370  0.10
  33.29000  -101.13000 0.729   -0.4043  0.10
  32.62000  -102.49000 0.966   -0.3115  0.10
  32.60000  -100.97000 0.676   -0.6798  0.10
  32.67000  -100.39000 0.622   -0.6130  0.10
  31.94000  -100.32000 0.574   -1.4324  0.10
  31.89000   -99.65000 0.621   -1.2890  0.10
  31.49000  -101.98000 0.842   -0.7615  0.10
  31.41000  -101.18000 0.742   -1.2278  0.10
  30.79000  -101.24000 0.768   -1.3416  0.10
  30.68000  -100.61000 0.700   -1.7028  0.10
```

Figure A.7. FMTOMO source file; this is an example of one event file. The first line indicates the number of receivers for which there are measured relative arrival times. The second line is the latitude, longitude, and depth of the event, respectively. The third line indicates the phase, and the following lines are the receiver latitudes, longitudes, elevation, relative arrival time, and its uncertainty, respectively.

```
         2           1
        24          47          47
  24.1904761904762        3.827824488733754E-003  3.887324351252931E-003
  5841.30952380952        0.481373721067653       -1.90280560336330
 9.76216000  0.30000000
 9.76216000  0.30000000
 9.76216000  0.30000000
 9.76216000  0.30000000
 9.76216000  0.30000000
 9.76216000  0.30000000
 9.76216000  0.30000000
 9.76216000  0.30000000
 9.76216000  0.30000000
 9.76216000  0.30000000
 9.76216000  0.30000000
 9.76216000  0.30000000
 9.76216000  0.30000000
 9.76216000  0.30000000
 9.76216000  0.30000000
 9.76216000  0.30000000
 9.76216000  0.30000000
 9.76216000  0.30000000
 9.76216000  0.30000000
 9.76216000  0.30000000
 9.76216000  0.30000000
```

Figure A.8. FMTOMO output file; this is the *vgrids.in* file created when the inversion is run. The first line indicates the number of velocity grids and the number of velocity types, respectively. The second line indicates the number of velocity nodes in depth, latitude, and longitude, respectively. The third line indicates the distance between nodes in depth (km), latitude (radians), and longitude (radians), respectively. The fourth line indicates the starting point of the velocity grid in km from Earth's center, latitude (radians), and longitude (radians), respectively. The following lines indicate the velocity at each node and its uncertainty, beginning at the base of the model, with longitude varying the fastest, and latitude varying the second fastest.

APPENDIX B

Depth Slices of the Compressional Model

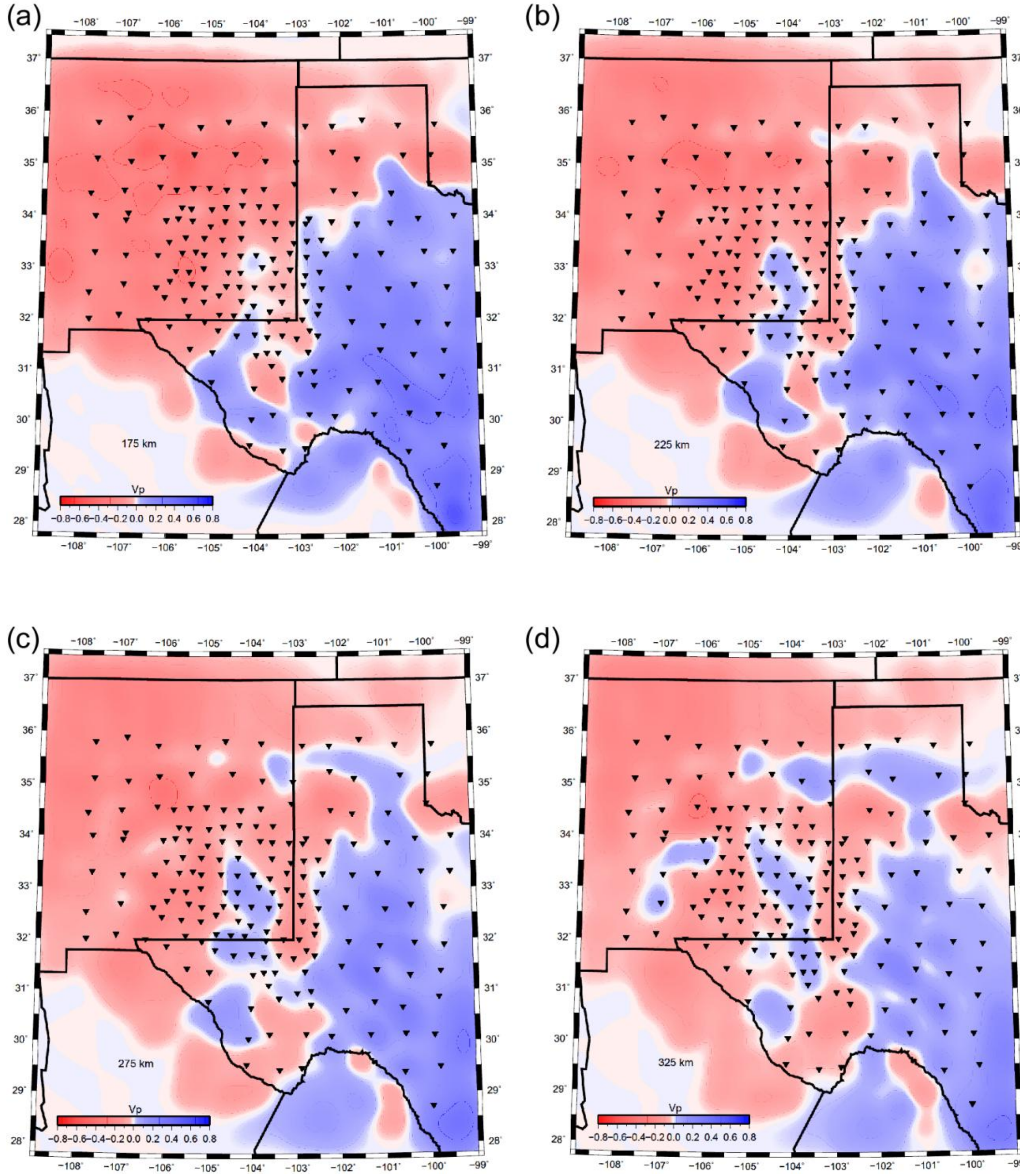

Figure B.1. Depth sections from the compressional model at (a) 175 km, (b) 225 km, (c) 275 km, and (d) 325 km.

APPENDIX C

Latitudinal Cross-sections of the Compressional Model

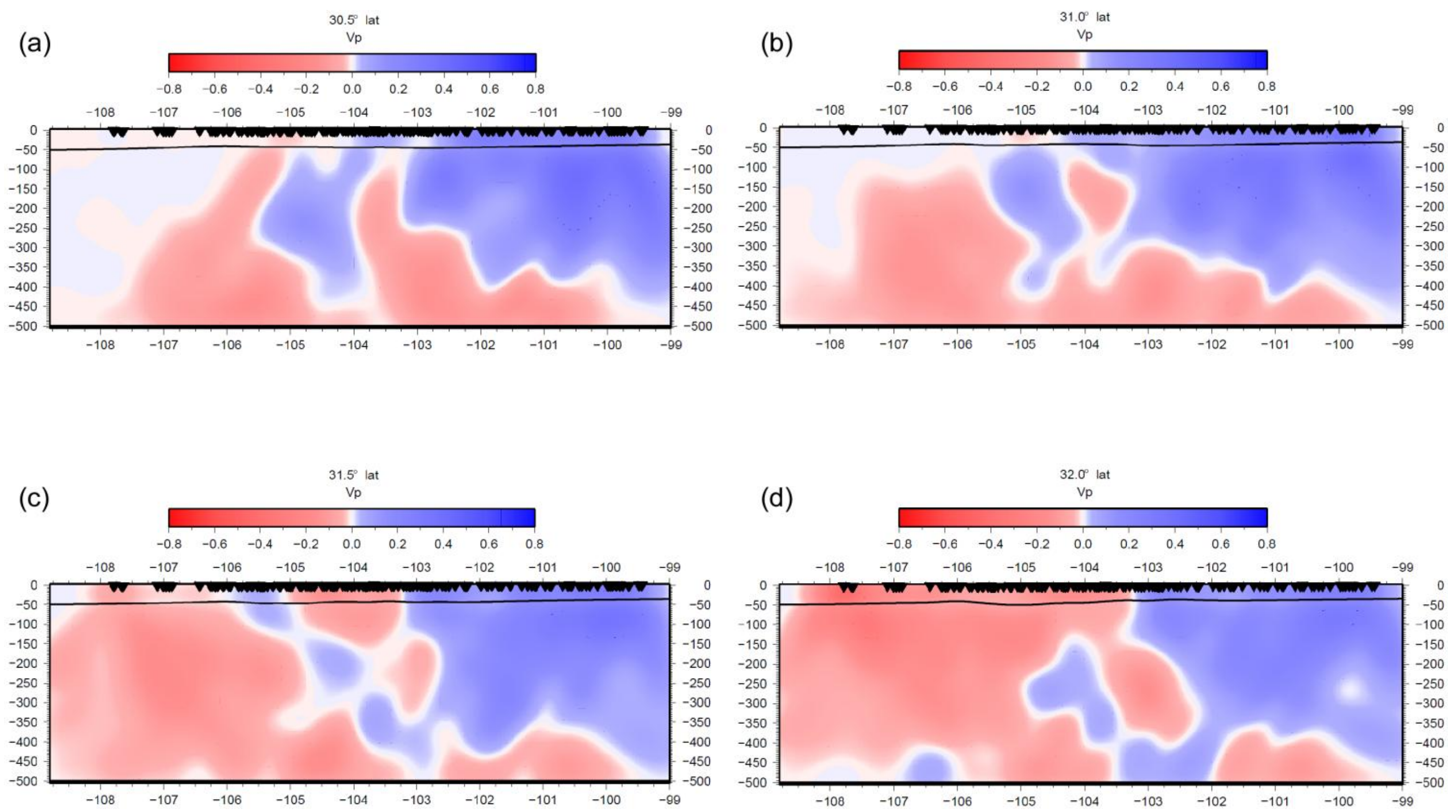

Figure C.1. Latitudinal cross-sections through the compressional model at (a) 30.5°, (b) 31.0°, (c) 31.5°, and (d) 32.0°.

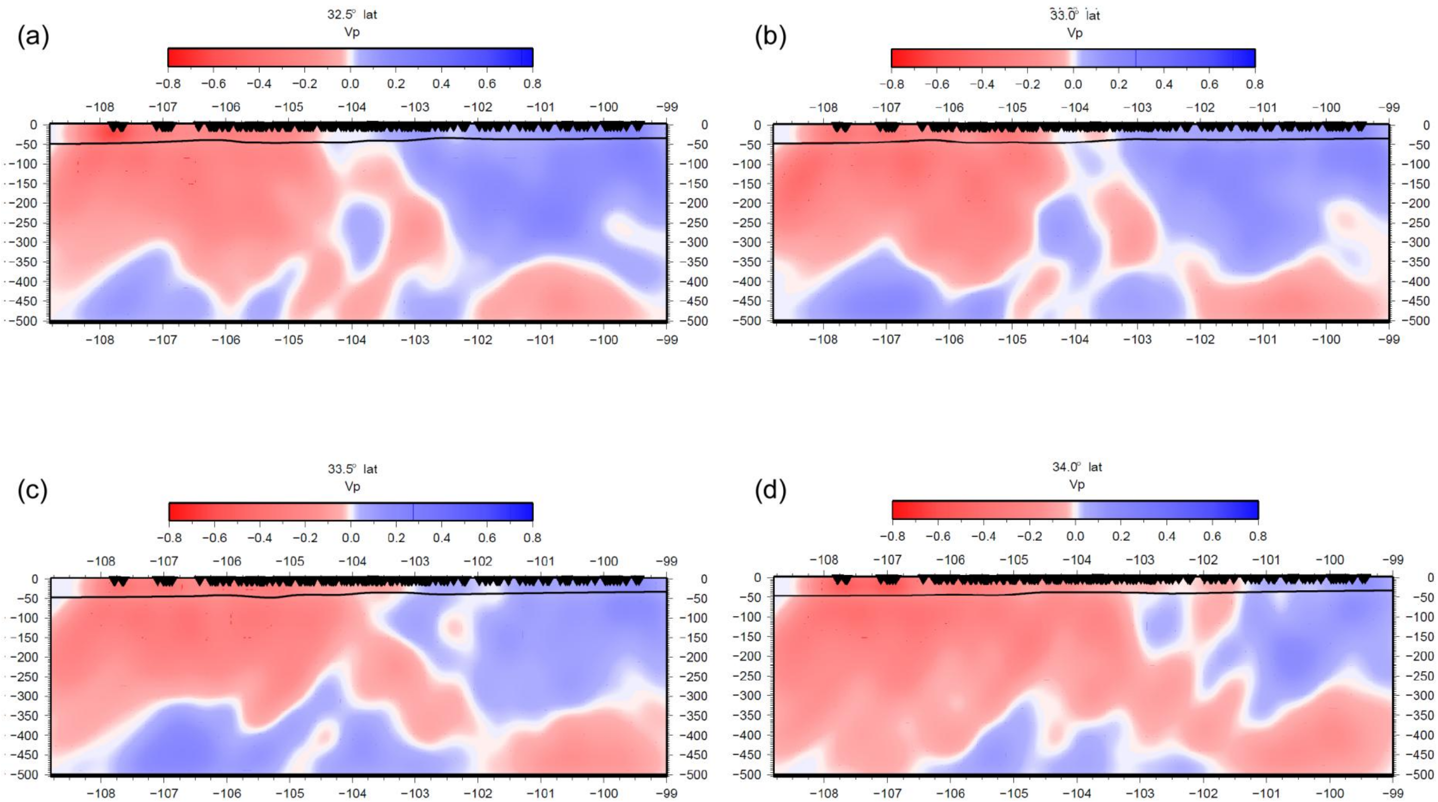

Figure C.2. Latitudinal cross-sections through the compressional model at (a) 32.5°, (b) 33.0°, (c) 33.5°, and (d) 34.0°.

APPENDIX D

Longitudinal Cross-sections of the Compressional Model

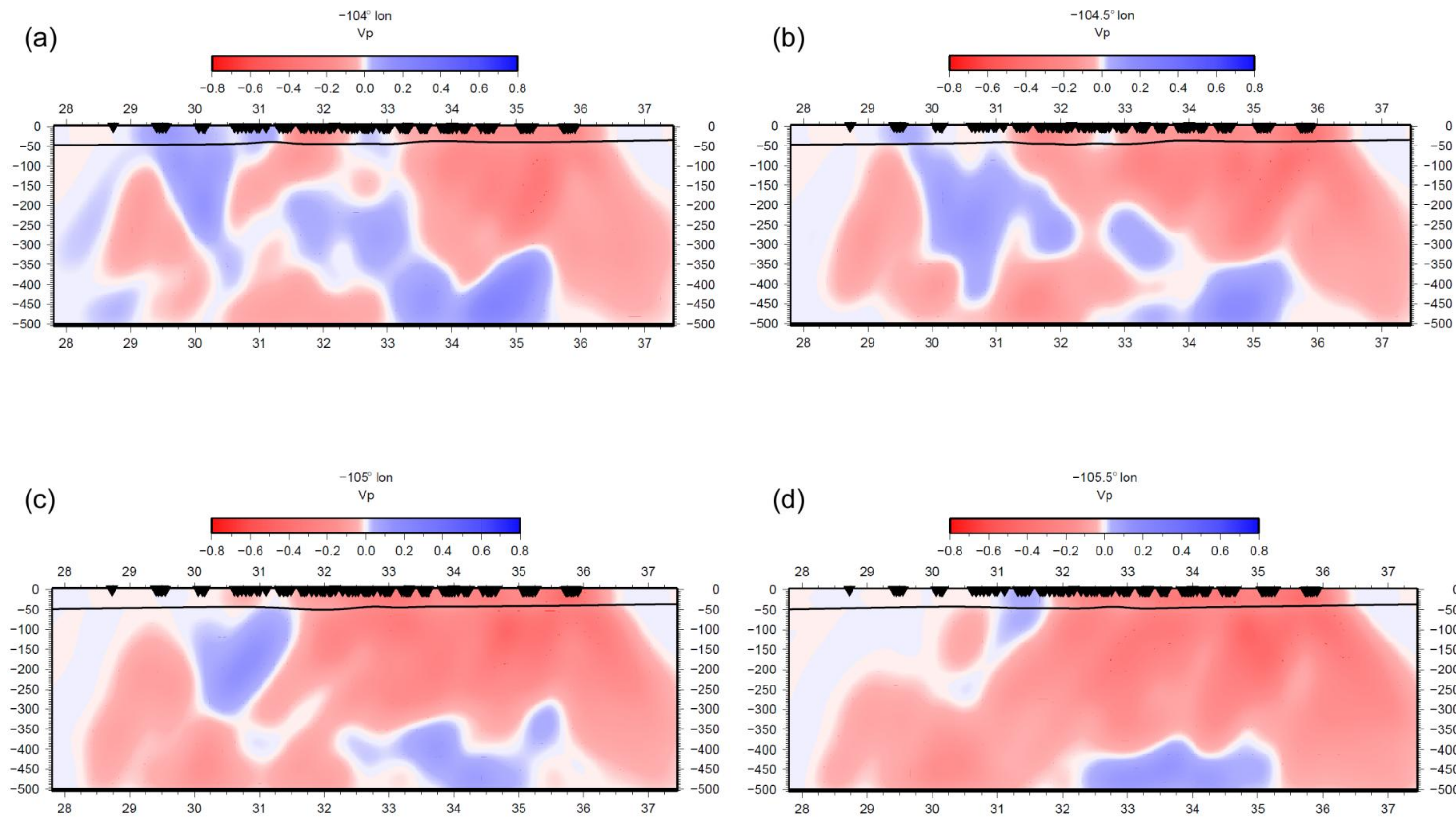

Figure D.1. Longitudinal cross-sections of the compressional model through (a) -102.0°, (b) -102.5°, (c) -103.0°, and (d) -103.5°.

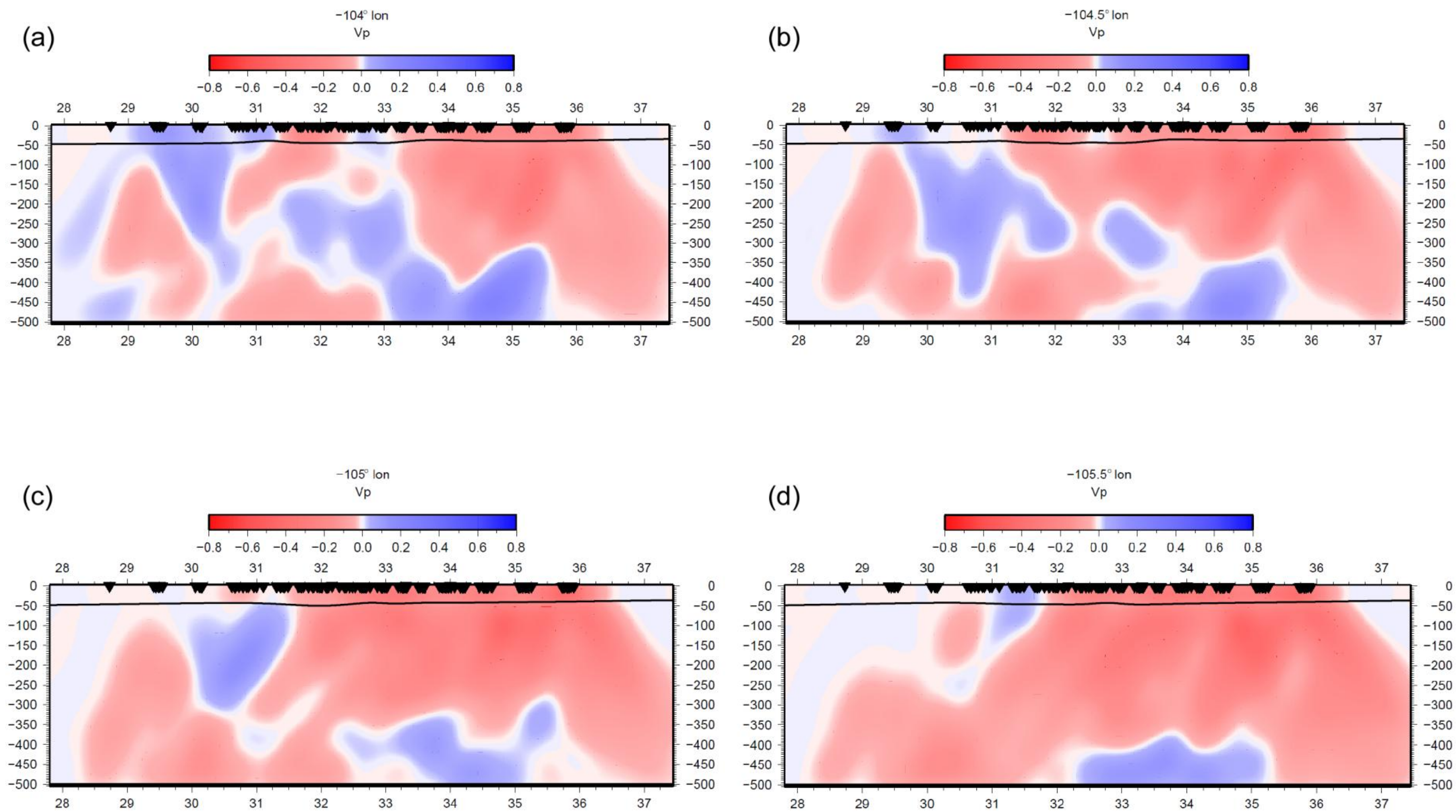

Figure D.2. Longitudinal cross-sections of the compressional model through (a) -104.0°, (b) -104.5°, (c) -105.0°, and (d) -105.5°.

APPENDIX E

Depth Slices of the Shear Model

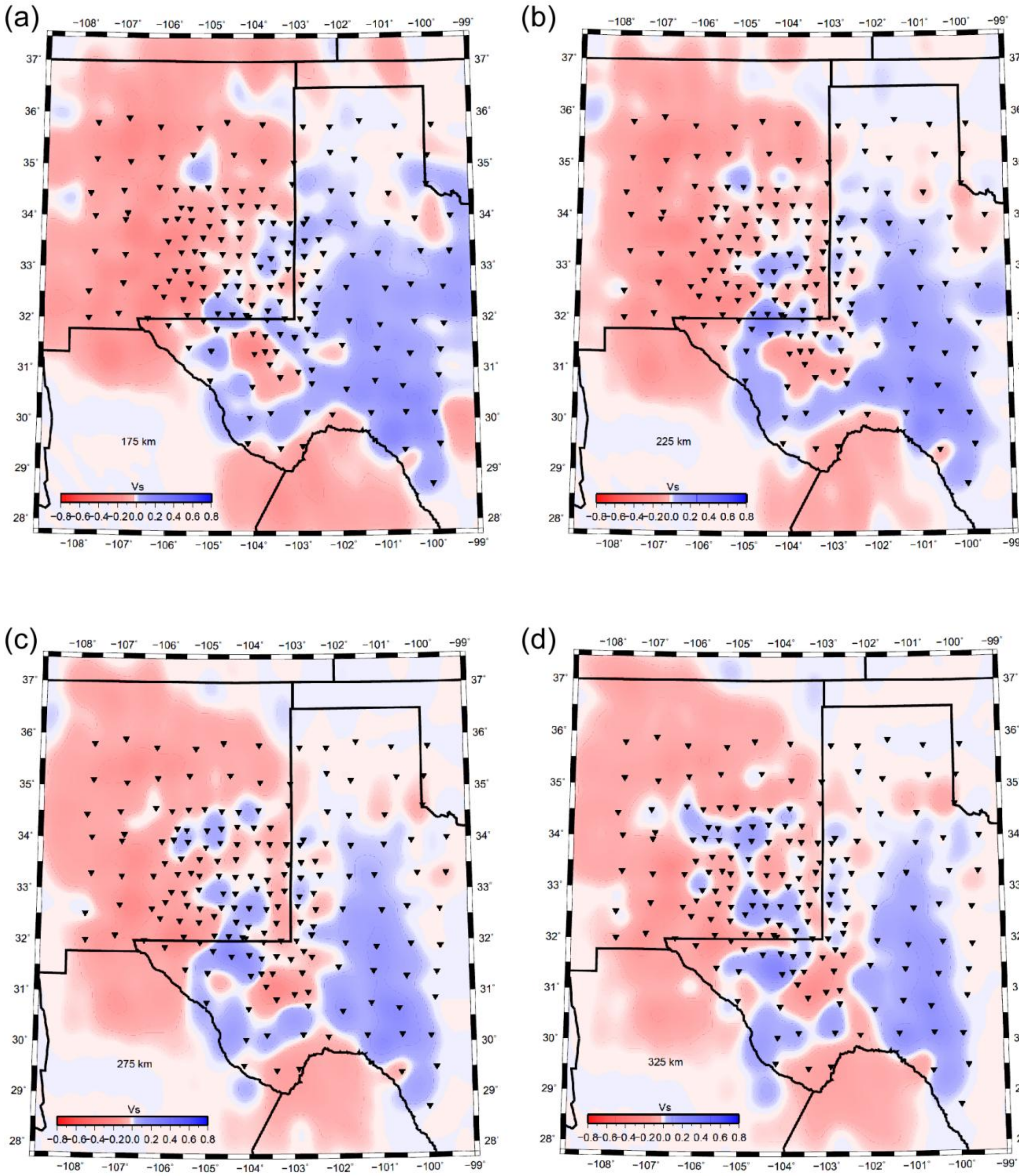

Figure E.1. Depth sections through the shear model at (a) 175 km, (b) 225 km, (c) 275 km, and (d) 325 km.

APPENDIX F

Latitudinal Cross-sections of the Shear Model

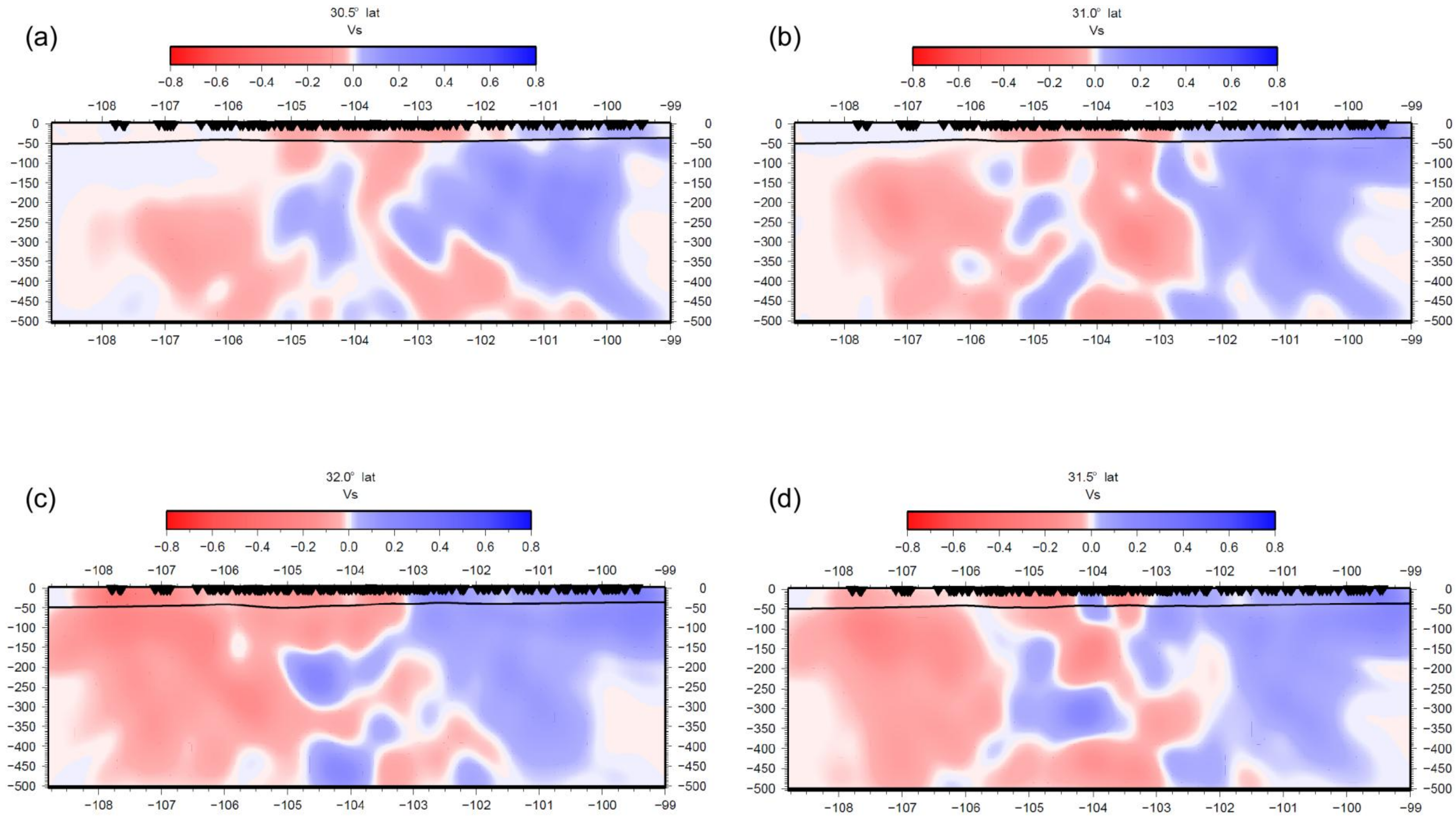

Figure F.1. Latitudinal cross-sections through the shear model at (a) 30.5°, (b) 31.0°, (c) 31.5°, and (d) 32.0°.

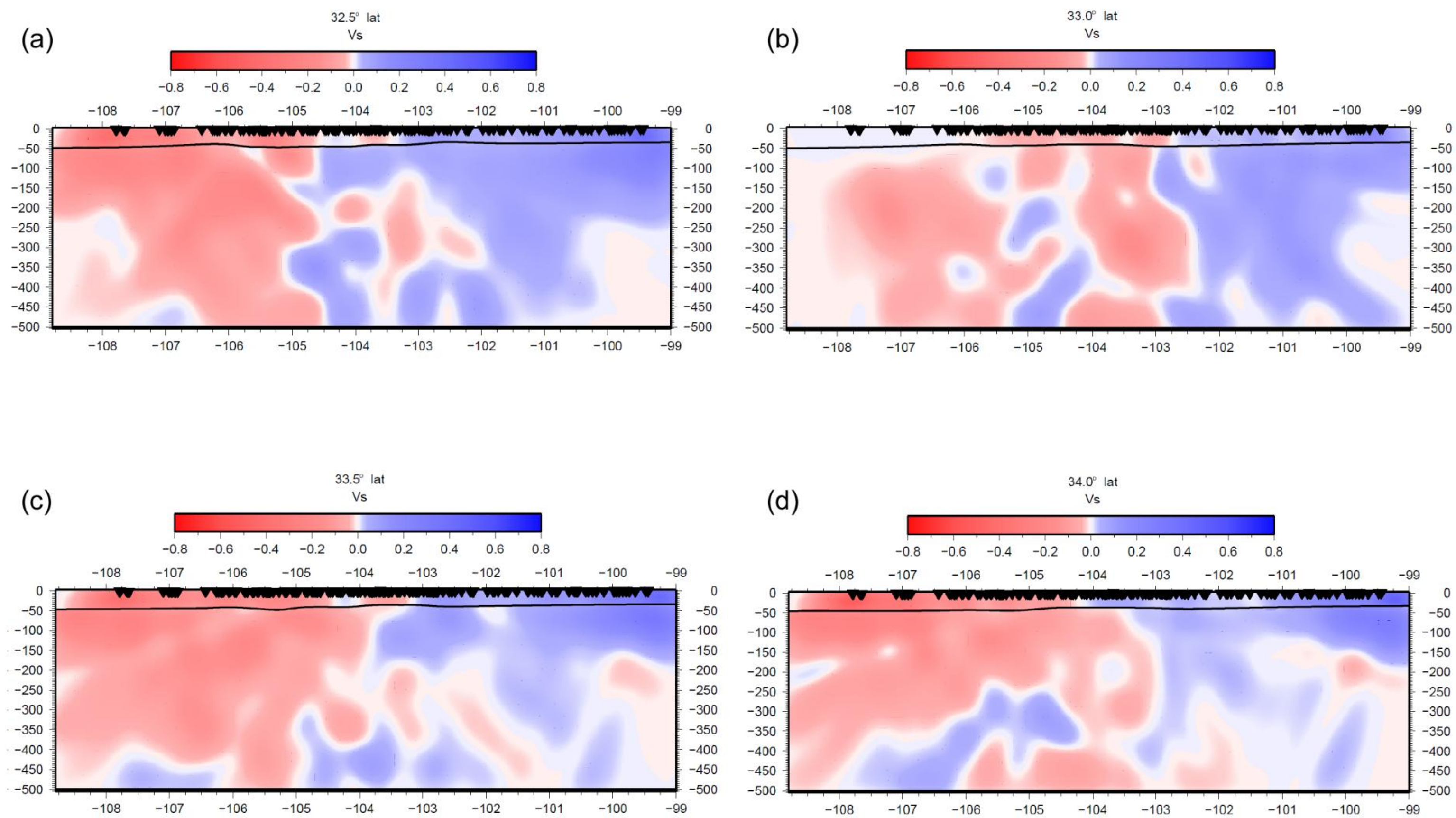

Figure F.2. Latitudinal cross-sections through the shear model at (a) 32.5°, (b) 33.0°, (c) 33.5°, and (d) 34.0°.

APPENDIX G

Longitudinal Cross-sections of the Shear Model

(a)

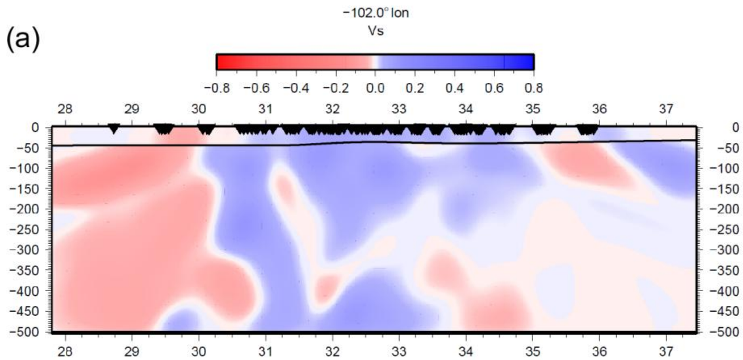

(b)

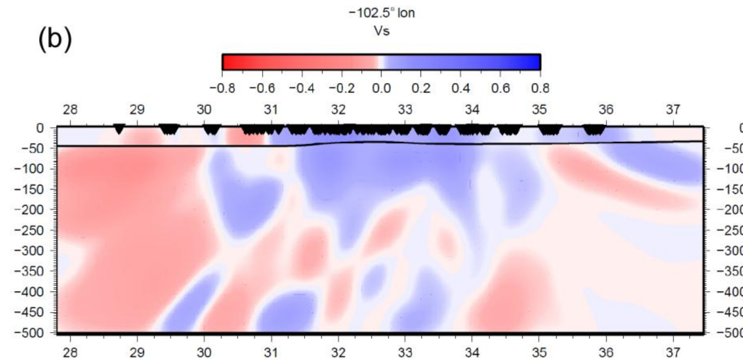

(c)

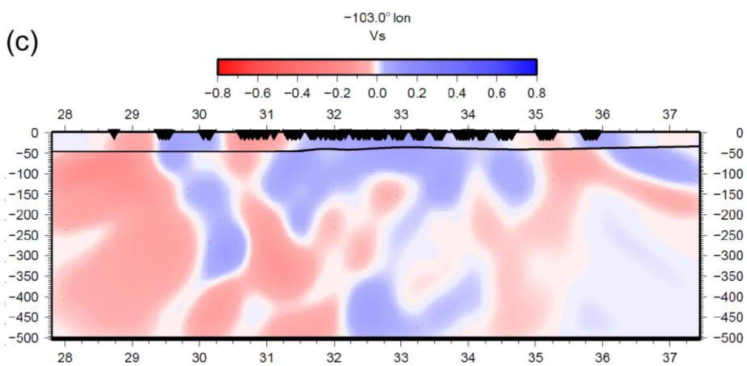

(d)

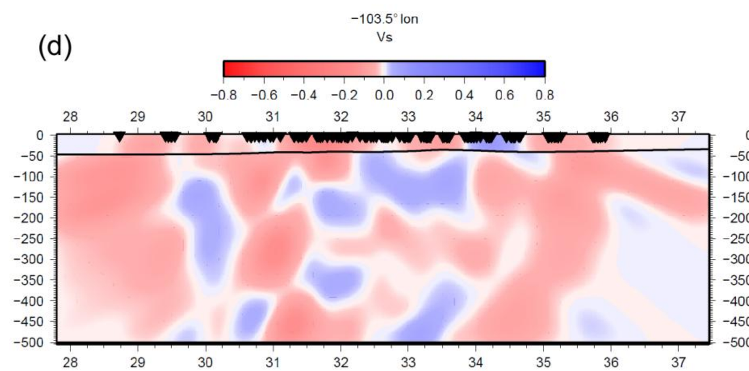

Figure G.1. Longitudinal cross-sections through the shear model at (a) -102.0°, (b) -102.5°, (c) -103.0°, and (d) -103.5°.

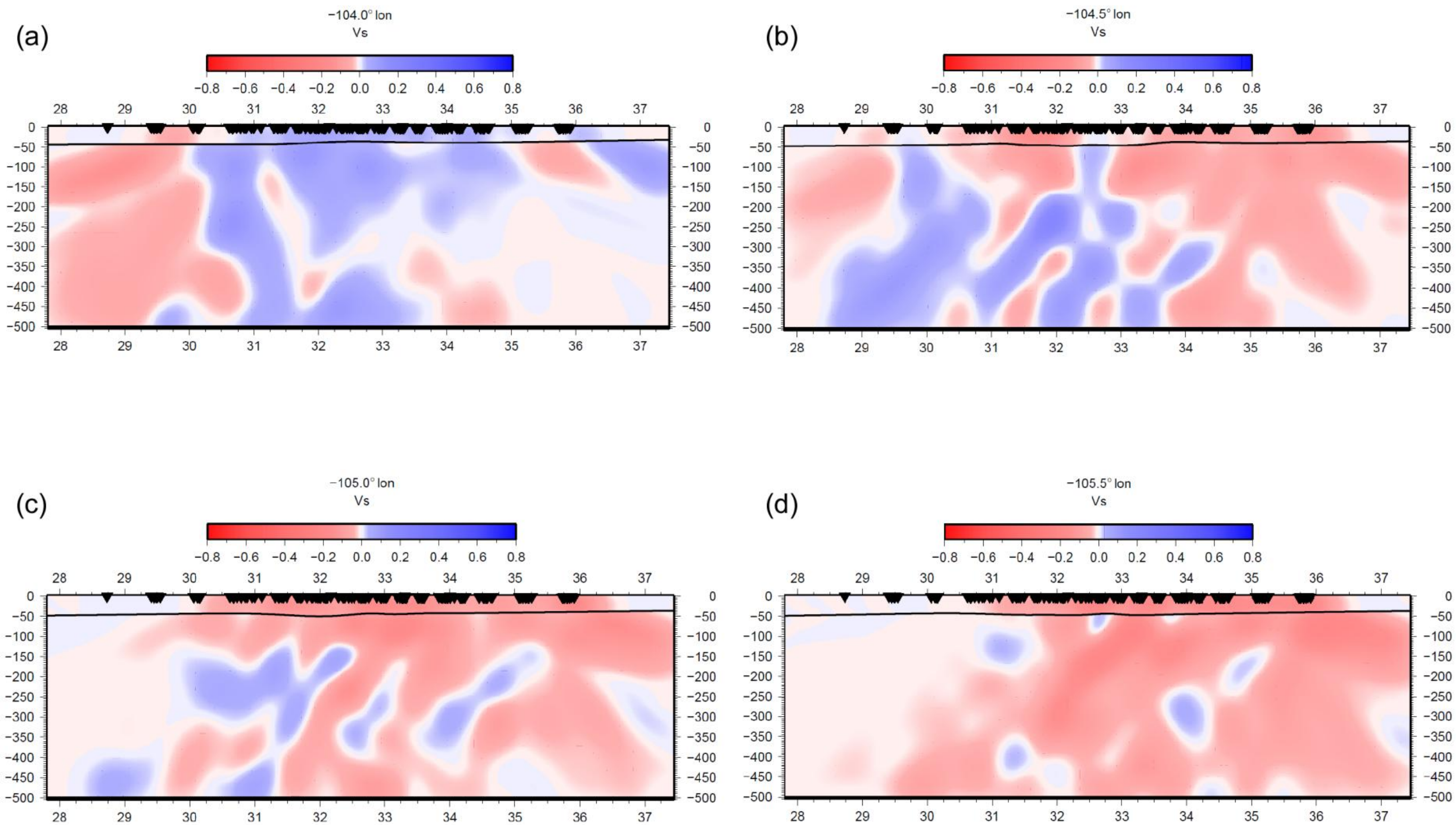

Figure G.2. Longitudinal cross-sections through the shear model at (a) -104.0°, (b) -104.5°, (c) -105.0°, and (d) -105.5°.

APPENDIX H

Compressional and Shear Isosurfaces

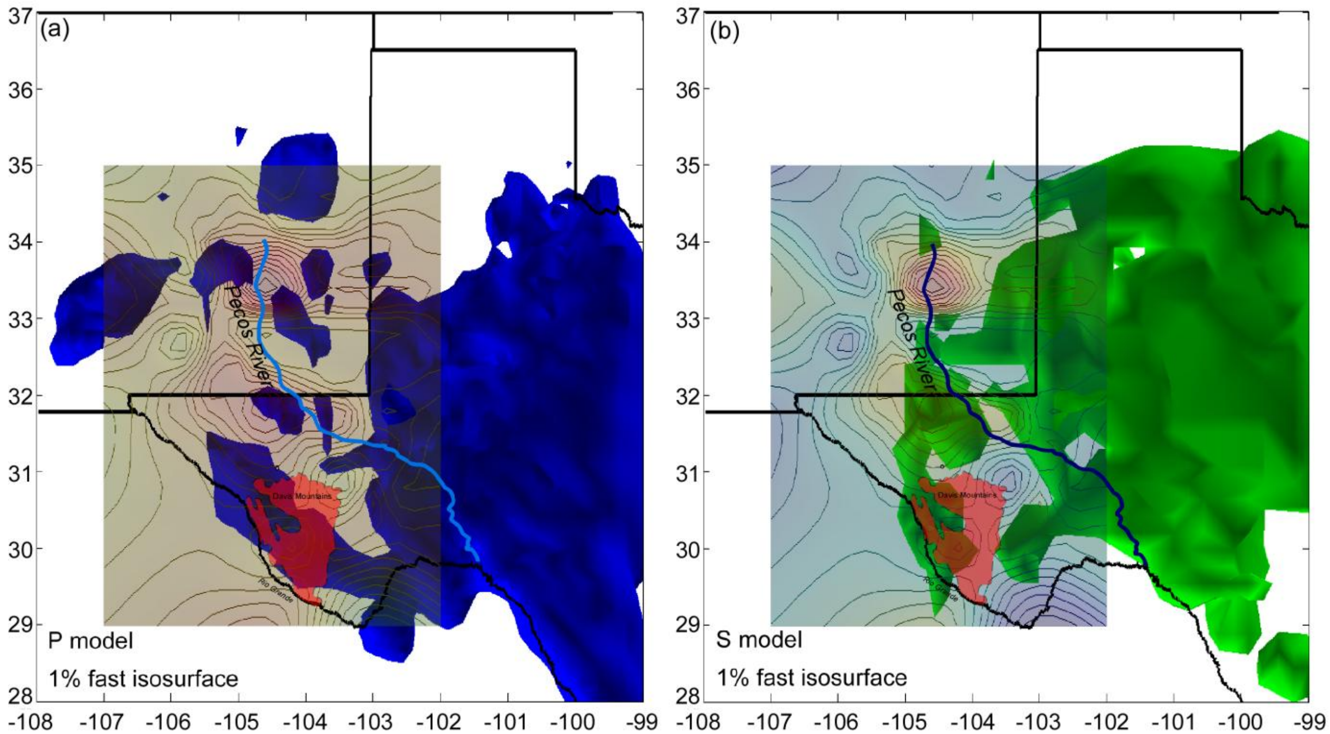

Figure H.1. (a) 1% fast isosurface of the compressional model. (b) 1% fast isosurface of the shear model. Contours represent Moho topography with two major depressions at ~33.5° and ~32.0° (Yu Xia, pers. comm., November 11, 2010). Davis Mountains correlate with a large portion of the anomaly in Texas and the Pecos River Valley correlates with a Moho depression and the anomaly in New Mexico.

APPENDIX I

Correlation of Regional Topography with Anomaly

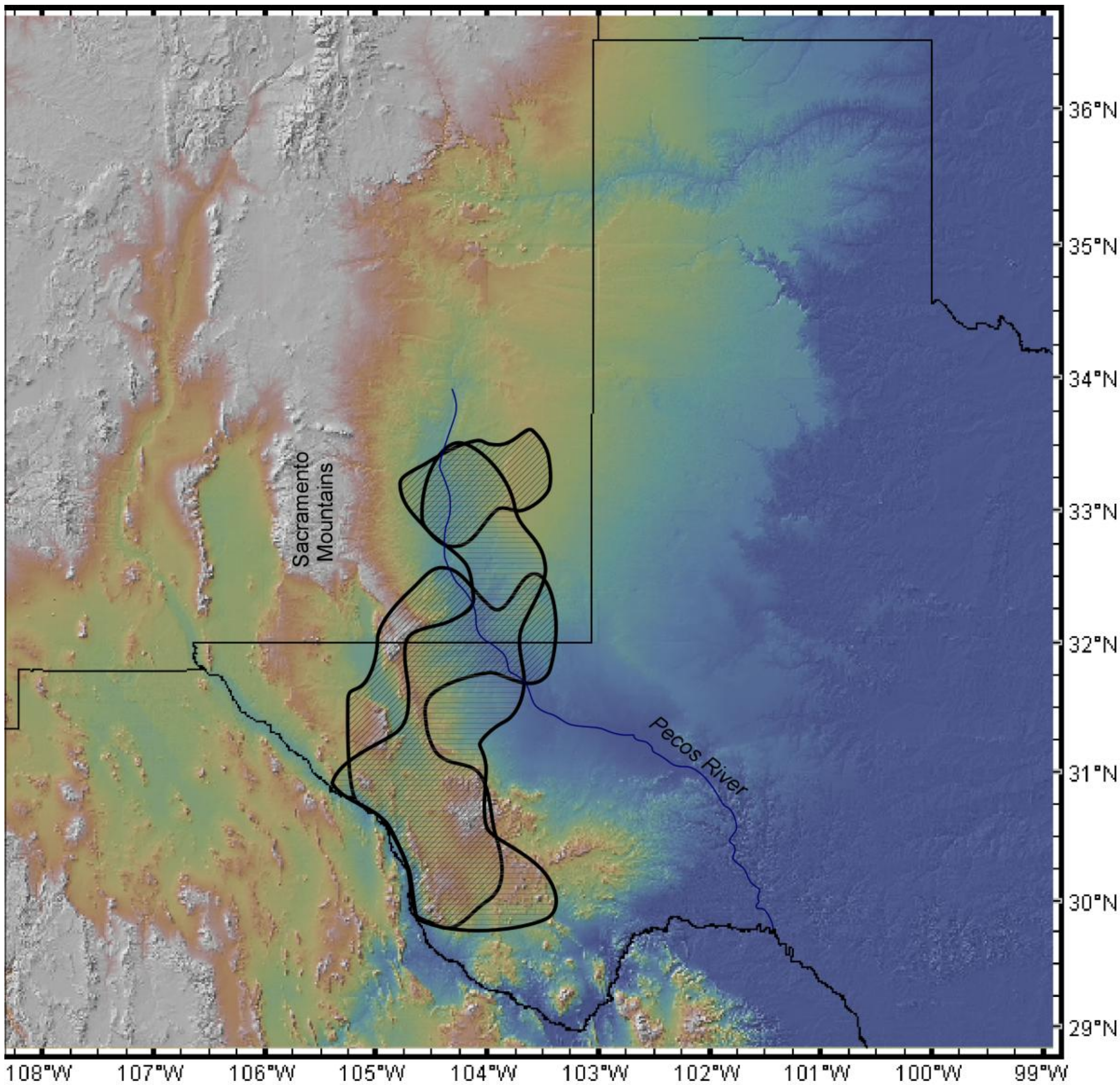

Figure I.1. The uplift of the Sacramento Mountains is possibly an effect of the sinking lithosphere. Shaded areas indicate the surface projection of the anomaly from P and S tomography at 225 km. Within New Mexico, the anomaly correlates spatially with the Pecos River Valley.

REFERENCES

Axelrod, D. I., and H. P. Bailey (1976), Tertiary vegetation, climate and altitude of the Rio Grande depression, New Mexico-Colorado, *Paleobiology, 2*, 235 – 254.

Baldridge, W. S., P. E. Damon, M. Shafiqullah, and R. J. Birdwell (1980), Evolution of the centrel Rio Grande rift, New Mexico: New potassium-argon ages, *Earth Planet. Sci. Lett., 51*, 309 – 321.

Baldridge, W. S., F. V. Perry, D. T. Vaniman, L. D. Nealey, B. D. Leavy, A. W. Laughlin, P. R. Kyle, Y. Bartov, G. Steintz, and E. S. Gladney (1991), Middle to late Cenozoic magmatism of the southeastern Colorado Plateau and central Rio Grande Rift (New Mexico and Arizona, U. S. A.): A model for continental rifting, *Tectonophysics*, *197*, 327 – 354.

Baldridge, W. S., G. R. Keller, V. Haak, E. Wendlandt, G. R. Jiracek, and K. H. Olsen (1995), The Rio Grande Rift, in *Continental Rifts: Evolution, Structure,Tectonics*, edited by K. H. Olsen, pp. 233 – 275, Elsevier, Amsterdam, The Netherlands.

Baltz, E. H. (1978), Resume of Rio Grande depression in north-central New Mexico, *Circ. N. M. Bur. Mines Miner. Resour.*, *163*, 210 – 228.

Barker, D.S. (1987), Tertiary alkaline magmatism in Trans-Pecos Texas. , *In Alkaline Igneous Rocks,* edited by J.G. Fitton and B.G.J.Upton, Geol. Soc.,Spec.Publ., *30*, 415 - 431.

Bird, P. (1978), Initiation of intracontinental subduction in the Himalaya, *J. Geophys. Res., 83,* 4975 – 4987.

Bird, P. (1979), Continental delamination and the Colorado Plateau, *J. Geophys. Res., 84,* 7561 – 7571.

Bird, P. and J. Baumgardner (1981), Steady propagation of delamination events, *J. Geophys. Res., 86,* 4891 – 4903.

Brown, C. D. and R. J. Phillips (1999), Flexural rift flank uplift at the Rio Grande rift, New Mexico, *Tectonics, 18*(6), 1275 – 1291.

Bunge, H.-P., and S. P. Grand (2000), Mesozoic plate-motion history below the northeast Pacific Ocean from seismic images of the subducted Farallon slab, *Nature*, *405*, 337 – 340.

Calzia, J. P., and W. L. Hiss (1978), Igneous rocks in northern Delaware Basin, New Mexico and Texas, in *Geology and mineral deposits of Ochoan rocks in Delaware Basin and adjacent areas*, edited by G. S. Austin, *New Mexico Bureau of Mines and Mineral Resources Circ., 159,* 39 – 45.

Chapin, C. E. (1979) Evolution of the Rio Grande rift – A summary, in *Rio Grande Rift: Tectonics and Magmatism*, edited by R. E. Riecker, pp. 1 – 5, AGU, Washington, D.C.

Chapin, C. E., and W. R. Seager (1975), Evolution of the Rio Grande Rift in the Socorro and Las Cruces areas, *New Mexico Geol. Soc. Guidebook, 26th Field Conf.*, Las Cruces Country, 297 – 322.

Clarkson, G., and M. Reiter (1984), Analysis of terrestrial heat flow profiles across the Rio Grande rift and southern Rocky Mountains in northern New Mexico, *N.M. Geol. Soc., Field Conf. Guideb., 35,* 39 – 44.

Coney, P. J., and S. J. Reynolds (1977), Cordilleran Benioff zones, *Nature*, *270*, 403 – 406.

Cordell, L. (1978), Regional geophysical setting of the Rio Grande rift, *GSA Bulletin, 89*(7), 1073 – 1090.

Cordell, L., G. R. Keller, and T. G. Hildenbrand (1982), Bouguer gravity map of the Rio Grande rift, Colorado, New Mexico, and Texas, *U. S. Geol. Surv.,* Map GP-949, 1:1,000,000.

Davis, P. M., P. Slack, H. A. Dahlheim, W. V. Green, R. P. Meyer, U. Achauer, A. Glahn, and M. Granet (1993), Teleseismic tomography of continental rift zones, in *Seismic Tomography – Theory and Practice,* edited by H. M. Iyer and K. Hirahara, Chapter 15, Chapman and Hall, 848 pp.

de Kool, M., N. Rawlinson, and M. Sambridge (2006), A practical grid-based method for tracking multiple refraction and reflection phases in three-dimensional heterogeneous media, *Geophys. J. Int.*, *167*, 253 – 270.

de Voogd, B., L. D. Brown, and C. Merey (1986), Nature of the eastern boundary of the Rio Grande rift from COCORP surveys in the Albuquerque basin, New Mexico, *J. Geophys. Res., 91,* 6305 – 6320.

de Voogd, B., L. Serpa, and L. Brown (1988), Crustal extension and magmatic processes: COCORP profiles from Death Valley and the Rio Grande rift, *Geol. Soc. Amer. Bull., 100,* 1550 – 1567.

Decker, E. R., and S. B. Smithson (1975), Heat flow and gravity interpretation across the Rio Grande rift in southern New Mexico and West Texas, *J. Geophys. Res., 80*(17), 2542 – 2552.

Decker, E. R., G. J. Bucher, K. L. Buelow, and H. P. Heasler (1984), Preliminary interpretation of heat flow and radio-activity in the Rio Grande rift zone in central and northern Colorado, *N.M. Geol. Soc., Field Conf. Guideb., 35*, 45 – 50.

Decker, E. R., H. P. Heasler, K. L. Buelow, K. H. Baker, and J. S. Itallin (1988), Significance of past and recent heat-flow and radioactivity studies in the southern Rocky Mountains region, *Geol. Soc. Amer. Bull.*, *100*, 1851 – 1885.

Dickinson, W. R., and W. S. Snyder (1978), Plate tectonics of the Laramide orogeny, *Mem. Geol. Soc. Am.*, *151*, 355 – 366.

Doin, M.-P., L. Fleitout, and U. Christensen (1997), Mantle convection and stability of depleted and undepleted continental lithosphere, *J. Geophys. Res.*, *102*(B2), 2771 – 2787.

Eaton, G. P. (1986), A tectonic redefinition of the Southern Rocky Mountains, *Tectonophysics*, *132*, 163 – 193.

Eaton, G. P. (2008), Epeirogeny in the Southern Rocky Mountains region: Evidence and origin, *Geosphere*, *4*(5), 764 – 784.

Gao, W., S. P. Grand, W. S. Baldridge, D. Wilson, M. West, J. F. Ni, and R. Aster (2004), Upper mantle convection beneath the central Rio Grande rift imaged by P and S wave tomography, *J. Geophys. Res.*, *109*, B03305, doi:10.1029/2003JB002743.

Girdler, R. W. (1975), The great negative Bouguer gravity anomaly over Africa, *EOS Trans., Amer. Geophys. Union*, *56*, 516.

Glahn, A., and M. Granet (1993), Southern Rhine Graben: small-wavelength tomographic study and implications for the dynamic evolution of the graben, *Geophys. J. Int.*, *113*, 399 – 418.

Golombek, M. P., G. E. McGill, and L. Brown (1983), Tectonic and geologic evolution of the Española Basin, Rio Grande rift: Structure, rate of extension, and relation to the state of stress in the western United States, *Tectonophysics*, *94*, 483 – 507.

Graeber, F. M., and G. Asch (1999), Three-dimensional models of *P* wave velocity and *P*-to-*S* velocity ration in the southern central Andes by simultaneous inversion of local earthquake data, *J. Geophys. Res.*, *104*, 20237 – 20256.

Griffin, W. L., S. Y. O'Reilly, B. J. Doyle, N. J. Person, H. Coopersmith, K. Kivi, V. Malkovets, and N. Pokhilenko (2004), Lithosphere mapping beneath the North American plate, *Lithos*, *77*, 873 – 922.

Ham, W. E., R. E. Denison, and C. A. Merritt (1965), Basement rocks and structural evolution of southern Oklahoma – a summary, *AAPG Bulletin*, *49*(7), 927 – 934.

Hearn, T. M., and R. W. Clayton (1986), Lateral velocity variations in southern California. I. Results for the upper crust from *Pg* waves, *Bull. Seism. Soc. Am.*, *76*, 495 – 509.

House, M. A., S. A. Kelley, and M. Roy (2003), Refining the footwall cooling history of a rift flank uplift, Rio Grande rift, New Mexico, *Tectonics, 22,* 1060 – 1078.

Humphreys, E. D. (1995), Post-Laramide removal of the Farallon slab, western United States, *Geology*, *23*, 987 – 990.

Karlstrom, K. E., and E. D. Humphreys (1998), Persistent influence of Proterozoic accretionary boundaries in the tectonic evolution of southwestern North America: Interaction of cratonic grain and mantle modification events, *Rocky Mountain Geology*, *33*(2), 161 – 179.

Keller, G. R., L. W. Braile, and J. W. Schlue (1979), Regional crustal structure of the Rio Grande rift from surface wave dispersion measurements, in *Rio Grande Rift: Tectonics and Magmatism*, edited by R. E. Riecker, Am. Geophys. Union, Spec. Publ.: 115 – 126.

Keller, G. R., and L. Cordell (1984), Bouguer gravity anomaly map of New Mexico, *Nat. Ocean. Atmos. Admin.*, Nat. Geophys. Data Center Map, 1:500,000.

Keller, G. R., and W. S. Baldridge (1999), The Rio Grande Rift: A geological and geophysical overview, *Rocky Mount. Geol., 34*, 121 – 130.

Kennett, B. L. N., M. S. Sambridge, and P. R. Williamson (1988), Subspace methods for large scale inverse problems involving multiple parameter classes, *Geophys. J.*, *94*, 237 – 247.

King, S. D., and J. Ritsema (2000), African Hot Spot Volcanism: Small-Scale Convection in the Upper Mantle Beneath Cratons, *Science*, *290*(5494), 1137 – 1140.

Lambert, D. D., D. M. Unruh, and M. C. Gilbert (1988), Rb-Sr and Sm-Nd isotopic study of the Glen Mountains layered complex: Initiation of rifting within the southern Oklahoma aulacogen, *Geology, 16,* 13 – 17.

Lee, C.-T., Q. Yin, R. L. Rudnick, and S. B. Jacobsen (2001), Preservation of ancient and fertile lithospheric mantle beneath the southwestern United States, *Nature*, *411,* 69–73.

Manley, K. (1979), Stratigraphy and structure of the Española Basin, Rio Grande rift, New Mexico, in *Rio Grande Rift: Tectonics and Magmatism*, edited by R. E. Riecker, pp. 71 – 86, AGU, Washington, D.C.

Manley, K., and H. H. Mehnert (1981), New K-Ar ages of Miocene and Pliocene volcanic rocks in northwestern Española Basin and their relationships to the history of the Rio Grande Rift, *Isochron West, 30*, 5 – 8.

McLemore, V. T., V. W. Lueth, T. C. Pease, and J. R. Guilinger (1996), Petrology and mineral resources of the Wind River Laccolith, Cornudas Mountains, New Mexico and Texas, *Can. Mineral.*, *34,* 335 – 347.

Molnar, P., and D. Gray (1979), Subduction of continental lithosphere: Some constraints and uncertainties, *Geology, 7*(1), 58 – 62.

Morency, C., M.-P. Doin, and C. Dumoulin (2002), Convective destabilization of a thickened continental lithosphere, *Earth Planet. Sci. Lett., 202*, 303 – 320.

Morgan, P., W. R. Seager, and M. P. Golombek (1986), Cenozoic thermal, mechanical, and tectonic evolution of the Rio Grande rift, *J. Geophys. Res.*, *91*, 6263 – 6276.

Murphy, B. P. (1991), Determination of shear wave velocity structure in the Rio Grande rift though receiver function and surface wave analysis, Ms. Thesis, University of Texas at El Paso, El Paso, Texas, 117 pp.

Olsen, K. H., G. R. Keller, and J. W. Stewart (1979), Crustal structure along the Rio Grande rift from seismic refraction profiles, in *Rio Grande Rift: Tectonics and Magmatism,* edited by R. E. Riecker, Am. Geophys. Union, Spec. Publ.: 127 – 143.

O'Reilly, S. Y., and W. L. Griffin (2006), Imaging global chemical and thermal heterogeneity in the sub-continental lithospheric mantle with garnets and xenoliths: Geophysical implications, *Tectonophysics*, *416,* 289 – 309.

Perry, F. V., W. S. Baldridge, and D. J. DePaolo (1988), Chemical and isotopic evidence for lithospheric thinning beneath the Rio Grande Rift, *Nature*, *332*, 432 – 434.

Popovici, A. M., and J. A. Sethian (2002), 3-D imaging using higher-order fast marching traveltimes, *Geophysics*, *67*, 604 – 609.

Price, J. G., C. D. Henry, D. S. Barker, and D. F. Parker (1987), Alkalic rocks of contrasting tectonic settings in Trans-Pecos Texas, in *Mantle Metasomatism and Alkaline Magmatism*, edited by E. M. Morris and J. D. Pasteris, *Geol. Soc. Am., Spec. Pap.*, *215*, 335 – 346.

Pulliam, J., C. V. Rockett, and S. P. Grand (2009), Seismic anisotropy of the Rio Grande rift and surrounding regions, *Am. Geophys. Union*, *Fall Meeting 2009,* Abstract No. T53D-1623.

Rawlinson, N., Fast *Marching Tomography Package: Instruction Manual*, Research School of Earth Sciences, Australian National University, Canberra ACT 0200. Retrieved May 2008, from http:// http://rses.anu.edu.au/~nick/fmtomo.html

Rawlinson, N., and B. L. N. Kennett (2008), Teleseismic tomography of the upper mantle beneath the southern Lachlan Orogen, Australia, *Phys. Earth Plane. Inter.*, *167*, 84 – 97.

Rawlinson, N., and M. Sambridge (2003), Seismic traveltime tomography of the crust and lithosphere, *Advances in Geophysics*, *46*, 81 – 197.

Rawlinson, N., and M. Sambridge (2004), Wave front evolution in strongly heterogeneous layered media using the fast marching method, *Geophys. J. Int.*, *156*, 631 – 647.

Rawlinson, N., A. M. Reading, and B. L. N. Kennett (2006), Lithospheric structure of Tasmania from a novel form of teleseismic tomography, *J. Geophys. Res.*, *111*, B02301, doi:10.1029/2005JB003803.

Reiter, M., C. L. Edwards, H. Hartman, and C. Weidman (1975), Terrestrial heat flow along the Rio Grande rift, New Mexico and southern Colorado, *Geol. Soc. Amer. Bull.*, *86*, 811 – 818.

Reiter, M., C. Shearer, and C. L. Edwards (1978), Geothermal anomalies along the Rio Grande rift in New Mexico, *Geology*, *6*(2), 85 – 88.

Reiter, M., A. J. Mansure, and C. Shearer (1979), Geothermal characteristics of the Rio Grande rift within the Southern Rocky Mountain complex, in *Rio Grande Rift: Tectonics and Magmatism*, edited by R. E. Riecker, *Am. Geophys. Union*, 253 – 267.

Reiter, M., and R. M. Chamberlin (2011), Alternative perspectives of crustal and upper mantle phenomena along the Rio Grande rift, *GSA Today*, *21*(2), 4 – 6.

Roy, M., J. K. MacCarthy, and J. Selverstone (2005), Upper mantle structure beneath the eastern Colorado Plateau and Rio Grande rift revealed by Bouguer gravity, seismic velocities, and xenolith data, *Geochem. Geophys. Geosyst.*, *6*(10), Q10007, doi:10.1029/2005GC001008.

Seager, W. R., and R. E. Clemons (1975), Middle to late Tertiary grology of the Cedar Hills-Seldon Hills area, New Mexico, *New Mex. Bur. Mines Min. Res. Circ. 133*, 24 p.

Seager, W. R., and P. Morgan (1979), Rio Grande Rift in southern New Mexico, West Texas, and northern Chihuahua, in *Rio Grande Rift: Tectonics and Magmatism*, edited by R. E. Riecker, pp. 87 – 106, AGU, Washington, D. C.

Seager, W. R., M. Shafiqulla, J. W. Hawley, and R. F. Marvin (1984), New K-Ar dates from basalts and the evolution of the southern Rio Grande rift, *Geol. Soc. Amer. Bull.*, *95*, 87 – 99.

Sethian, J. A. (1996), A fast marching level set method for monotonically advancing fronts, *Proc. Natl. Acad. Sci.*, *93*, 1591 – 1595.

Sethian, J. A. (2001), Evolution, implementation, and application of level set and fast marching methods for advancing fronts, *J. Comp. Phys.*, *169*, 503 – 555.

Sethian, J. A., and A. M. Popovici (1999), 3-D traveltime computation using the fast marching method, *Geophysics*, *64*, 516 – 523.

Sinno, Y. A., and G. R. Keller (1986), A Rayleigh Wave dispersion study between El Paso, Texas and Albuquerque, New Mexico, *J. Geophys. Res.*, *91*, 6168 – 7174.

Sinno, Y.A., P. H. Daggett, G. R. Keller, P. Morgan, and S. H. Harder (1986), Crustal structure of the southern Rio Grande rift determined from seismic refraction profiling, *J. Geophys. Res.*, *91*, 6143 – 6156.

Smith, D. L., and R. L. Jones (1979), Thermal anomaly in northern Mexico: An extension of the Rio Grande rift?, in *Rio Grande Rift: Tectonics and Magmatism*, edited by R. E. Riecker, pp. 269 – 278, Am. Geophys. Union, Spec. Pub.

Song, T.-R. A., and D. V. Helmberger (2007), P and S waveform modeling of continental sub-lithospheric detachment at the eastern edge of the Rio Grande Rift, *J. Geophys. Res.*, *112*, B07319, doi:10.1029/2007JB004942.

Swanberg, C. A. (1979), Chemistry of thermal and non-thermal groundwaters in the Rio Grande rift and adjacent tectonic provinces, in *Rio Grande Rift: Tectonics and Magmatism*, edited by R. E. Riecker, pp. 279 – 288, Am. Geophys. Union, Spec. Pub.

Thomas, R. G. (1972), The geomorphic evolution of the Pecos River system: Baylor Geological Studies Bull. 22, Baylor University, Waco, Texas, 40 p.

van Wijk, J. W., J. van Hunen, and S. Goes (2008), Small-scale convection during continental rifting: Evidence from the Rio Grande rift, *Geology*, *36*(7), 575 – 578.

Wessel, P., and W. H. F. Smith, 1995 New Version of the Generic Mapping Tools Released, EOS Trans. AGU, 76, p. 329

West, M., J. Ni, W. S. Baldridge, D. Wilson, R. Aster, W. Gao, and S. Grand (2004), Crust and upper mantle shear wave structure for the southwest United States: Implications for rifting and support for high elevation, *J. Geophys. Res.*, *109*, B03309, doi:10.1029/2003JB002575.

Wilson, D., R. Aster, M. West, J. Ni, S. Grand, W. Gao, W. S. Baldridge, S. Semken, and P. Patel (2005a), Lithospheric structure of the Rio Grande rift, *Nature*, *433*, 851 – 854.

Wilson, D., R. Aster, J. Ni, S. Grand, M. West, W. Gao, W. S. Baldridge, and S. Semken (2005b), Imaging the seismic structure of the crust and upper mantle beneath the Great Plains, Rio Grande Rift, and Colorado Plateau using receiver functions, *J. Geophys. Res.*, *110*, B05306, doi:10.1029/2004JB003492.